

Monitoring Mars with the Hubble Space Telescope:
1990-91 Observations

Philip B. James¹, Todd R. Clancy², Steven W. Lee^{*}, Leonard J. Martin³, Robert B. Sinaev⁴, Ed Smith⁵, Ralph A. Kahn⁶, and Richard P. Zurek⁶

¹ Department of Physics and Astronomy, University of Toledo, Toledo, OH 43606: 419-537-4906, FAX 419-537-2723

² LASP, University of Colorado, Boulder, CO 80309: 303-492-6998, FAX 303-492-6946

³ Lowell Observatory, 1400 West Mars Hill Rd., Flagstaff, AZ 86001: 602-774-3358

⁴ LPL, University of Arizona, Tucson, AZ: 602-621-4573, FAX 602-621-4933

⁵ Space Telescope Science Institute, Baltimore, MD

⁶ Jet Propulsion Laboratory, 4800 Oak Grove Dr., Pasadena, CA 91109

37 pages, 6 tables, 18 figures (23 individual photos and drawings)

Subject headings: Mars, Atmosphere; Mars, Surface; Meteorology

HST Mars Observations . . .

Send Correspondence to:

Philip B. James
Department of Physics and Astronomy
University of Toledo
Toledo, OH 43606
419-537-4906
FAX 419-537-2723
E mail: pjames@hubble.phya.utoledo.edu

Abstract

Images of Mars obtained using the Planetary Camera on the **Hubble** Space Telescope during 1990 and 1991 are described and analyzed. Multi-spectral images of Mars record the martian season between $L_s = 348$ and 60 corresponding to late winter and spring in the northern hemisphere. The wavelengths of these observations varied between 230 nm in the ultraviolet and 890 nm in the near infrared. We use these images to discuss atmospheric and polar phenomena, to constrain the aerosols and ozone in the martian atmosphere, and to compare surface **albedo** features within this data set as well as with previous observations.

Our observations are consistent with a Mars which is quite different from the planet viewed by Viking. The atmosphere was clear, and there was little evidence of dust storms on the planet. Despite this major difference, the behaviors of condensate clouds and the recession of the north polar cap are consistent with those observed by Viking. The quality of the images produced by HST, even when Mars subtended less than 5 arc seconds, confirms the potential value of HST observations in providing continuous synoptic coverage of the planet.

1. Introduction

The Wide Field / Planetary Camera (WFPC) of Hubble Space Telescope (HST) is in many ways an ideal instrument for synoptic scale observations of the planets. The nominal pixel scale of the Planetary Camera, .044 arc sees per pixel, provides a resolution on Mars near opposition which is similar to the approach pictures obtained by the Viking orbiters; at a favorable opposition, the scale at the sub earth point would approach 12 km per pixel. Even when Mars is small, 3-5 arc seconds, as it is during the largest part of its synodic cycle, the potential resolution of the Planetary Camera is as good as Planetary Patrol photographs acquired with good seeing conditions. In principle, this allows monitoring of phenomena on Mars throughout its synodic cycle although, in practice, HST observations are restricted to the period when the elongation of Mars from the sun exceeds 50 degrees in order to prevent accidental exposure of instruments to solar illumination. This is still a large improvement over conventional observations which have been generally limited to the period around opposition when the angular size of Mars is larger than 10 arc seconds or so for useful information.

Increasing the portion of the martian year during which synoptic changes can be resolved is important because such data are needed to disentangle the various time scales of large scale changes on the planet. The most historically significant example involves the large scale **albedo** changes observed on the planet. These were previously thought to be mostly seasonal changes, but the limitation of useful observations to the limited time periods near oppositions made it difficult to disentangle changes on a seasonal timescale from those due to interannual variability.

The other unique capability of HST is providing high spatial resolution images in the ultraviolet portion of the spectrum. Imaging and spectroscopy in the 200-350 nm wavelength region is uniquely suited to studies of ozone, dust, and clouds in the martian atmosphere. These measurements cannot be obtained from earth because of stratospheric ozone absorption, and no other spacecraft can provide comparable data. Both WFPC images in the UV portion of the spectrum and Faint Object Spectrograph (FOS) spectra have been used to study the martian atmosphere; the latter measurements will be reported elsewhere.

This article describes a group of observations of Mars by Hubble Space Telescope obtained between December 13, 1990 and May 15, 1991. The major goals of this program were to observe atmospheric and surface phenomena on the planet, to compare the observations with previous spacecraft and telescopic observations during the same season, to constrain the state and composition of the

atmosphere using ultraviolet observations, and to establish the value of HST observations for providing regular synoptic monitoring of Mars. The observations acquired are described in more detail in Section 2; Section 3 presents specifics about the data reduction techniques used with these images. The remainder of the paper describes and analyzes the observations as they relate to clouds and polar phenomena (Section 4), condensate and dust aerosols in the atmosphere (Section 5), radiative transfer modeling (Section 6) and surface **albedo** features (Section 7). Major conclusions are summarized in Section 8.

2. Observations

Because HST is not dependent on terrestrial weather or seeing conditions, an observational program can be planned with a good assurance of its successful completion. In reality, of course, time on HST is oversubscribed. The requirements which must be satisfied to achieve the research goals are not always compatible with scheduling constraints, and sequences must be designed within a finite time allocation. The various parameters which must be determined within this contest are the filters used, the number of exposures for any single **"target,"** the longitudinal coverage of the surface of the planet, and the timing and spacing of individual sequences or targets.

The principal series of filters available with the WFPC instrument are W (wide), a sequence of filters having widths ≈ 100 nm (e.g. photometric series), M (medium bandpass) filters with widths of a few tens of nm, and N (narrow) filters which are usually chosen for particular spectral features and which have widths of a few nm. For wavelengths in excess of 500 nm, Mars is sufficiently bright to saturate the W and M filters even with the shortest possible exposure times; these filters could be used with a supplementary neutral density filter but with associated additional difficulties with flat fields. Therefore, only N filters were used for these wavelengths; exposure times were typically a few tenths of a second, minimizing problems associated with spacecraft jitter and tracking. The latter was an important consideration because at the time these sequences were performed the solar system target software was not functioning, and all of the observations had to be programmed as fixed targets. The large proper motion of Mars would have caused smearing for longer observations. Although the 413M filter was chosen for our standard **"violet"** filter, 439W was substituted for the first set of observations at the suggestion of Space Telescope Science Institute (**STScI**) staff because these were taken before the W flood, which was most important for the instrument sensitivity at wavelengths around **400nm**. Much longer exposures were necessary for the 230W W filter because of reduced solar flux and reduced Mars reflectivity at the *w* wavelengths; special sequences to compensate for **Mars'** motion were designed by **STScI** personnel for those exposures. Several sequences in which a solar type star was to be imaged to provide both external

calibration for our filter combinations and point spread functions for **deconvolution** failed, and we therefore relied on internal WFPC calibrations in this work. The properties of the filters used are summarized in Table I.

HST has an orbital period of about 96 minutes. A near equatorial object such as Mars can be observed for approximately 45 minutes each orbit, sufficient to obtain a sequence of 6 or 7 exposures. In principal, Mars could be imaged on consecutive orbits during **Mars'** rotational period to provide 15 sequences separated by about 25 degrees of longitude. However, the necessary time would have more than exhausted the total time allocation. We therefore adopted a strategy of targeting a small number of global observations, limited to three central meridians separated by approximately 120 degrees, in addition to several monitoring sequences focused on a single central meridian on the planet. The first global sequence was obtained in December, 1990, shortly after opposition; another was done in mid-May, just before the elongation fell below 50 degrees and during a martian season when interesting clouds were expected to form. In principle, the global sequences could be mosaiced together to provide a complete global image, although with variable resolution. For the monitoring sequences, the region centered at 300 degrees longitude was chosen because this face of Mars includes two of the major variable **albedo** areas on the planet, **Syrtis Major** and **Hellas**, and several meteorologically interesting regions including **Hellas, Elysium**, and Arabia.

The number of filters also varied from sequence to sequence. The full complement was used only during the December opposition observations; typical monitoring sequences, on the other hand, utilized only red (673 N), blue (**413M**), and occasionally green (**502N**) or *w* pair (**336W, 230W**) filters. Table II contains a list of all WFPC observations. Ephemeris values are for the blue (439W and **413M**) images in the sequences. All of the images except the first opposition sequence were successfully obtained. In the first set of observations the image of Mars was formed partially off of the CCD chip so that only one-half to one-third of the planet was imaged. Because of the distortions and blemishes near the edge of the chip, those images were considered to be of little value. Figure 1 displays a montage of the 673N and 413M images of the Syrtis Major face of Mars discussed in this paper. The F439W and F673N December, 1990 opposition images are shown in Figure 2. The F673N image of **Solis** Lacus was acquired approximately 1.5 hours later than the F439N image because the spacecraft passed through the South Atlantic anomaly during the intervening time period.

3. Data Reduction

Targets were chosen so that the image of Mars appeared as close as possible to the center of **PC 6**, the best behaved of the four Planetary **Camera** CCD chips. Because the observations were designed

in groups of three at fixed target **co-ordinates**, the image shifted by substantial amounts across the chip. Fortunately, the ≈ 100 pixel borders where the chip is poorly behaved were generally avoided. In the highest resolution images, near opposition, the diameter of Mars is 370 pixels, slightly less than half of the chip width.

Procedures described by Lauer et al. (1989) were used for bias subtraction and flat fielding. However, due to the fact that we were among the first programs executed by **HST**, flat fields were not yet available for most of the filters which we used. Flats for some of the filters were obtained for use in our initial analysis through the courtesy of James Westphal and the WFPC team. More recently, flat fields for all but two of the filters (**588N** and **413M**) have been obtained by the WFPC team as part of the science verification process. The flat fields are developed from individual images of the bright earth; the WFPC team did obtain appropriate 413M exposures for us, and we have been able to combine these into a reasonably satisfactory flat for that filter. The **588N**, December, 1990 observations have continued to be analyzed using the flat originally supplied by Westphal. Cosmic rays were identified and removed by replacing the outstanding pixel with a mean of the surrounding region.

Division by the flat field normalizes out the large scale sensitivity variations in the filter / chip combination and removes much of the small scale structure (blemishes) which are mostly due to diffraction caused by dust on the filter and optical elements. However, when the intensity changes rapidly, as near the limb of Mars, many of the features still show up weakly in the flat fielded image. Because these blemishes have a scale similar to the **martian** features of interest and are enhanced by deconvolution, they must be carefully removed by hand. First, suspected blemishes are correlated with the relevant flat field image to make sure that they are due to system effects. The blemished region is then replaced with a smooth, two dimensional polynomial fit to the region surrounding the blemish to which appropriate noise has been added. In a few cases, blemishes have coincided with expected features; these must be given special attention. Following this procedure, a **"clean"** image is **obtained**; an **example** is shown in Figure 3a. For a more detailed description of this procedure see James et al. (1991) .

Because of the well-known spherical aberration problem encountered with the Optical Telescope Assembly (**OTA**), only about 12 % of the light is concentrated in the central 0.1 arc sec of the image of a point source. This is only about 20% of the amount expected. The remainder of the light is spread throughout a region comparable to the size of the planet; about 90% of the energy is within 1.6 sees of the center. Therefore, each point in the **"clean"** image in Figure 3 is a superposition of significant light from several thousand pixels in the desired image. This is especially evident

in the very diffuse limbs on the corrected raw images.

Fortunately, the mathematical problem of **deconvolving** the point spread function (**PSF**), the WFPC image of a point source, and the true planetary image is tractable. There are various techniques for performing the **deconvolution** of the images; we have used the Richardson-Lucy method (Lucy, 1974) which has found frequent application in the study of WFPC images. Because the **signal-to-noise** ratio of these images is so high (≈ 100), several iterations of the Lucy Richardson implementation in the STSDAS package restore most of the **original** sharpness to the images without producing excessive noise; forty to sixty iterations was generally optimum with further iterations increasing noise without significant improvement in resolution.

One requirement for the deconvolution procedure is a suitable point spread function (**PSF**) to use as the kernel for the transformation. One can either use well exposed stellar images as input or rely on computer simulations of the OTA and WFPC to generate **PSF's** numerically. Several attempts to obtain experimental PSFS using our filter set failed due to under-exposure (the central portion must be essentially saturated in order to expose the wings), safing events, and incorrect targeting. We have therefore relied entirely on PSFS generated by STSCI's "**Tiny Tim**" routine to deconvolve the images used here. Inasmuch as the images are located in various portions of the chip, as described earlier, this has the advantage of allowing the spatial dependence of the PSF to be considered; we did not, however, attempt to use multiple PSFS on these images. "**Tiny Tim**" also takes temporal changes in the position of the secondary mirror into account, thereby eliminating time-dependent effects. As an example, the deconvolved version of the image shown in Figure 3a is shown in Figure 3b.

In an effort to understand the effects of the aberration and subsequent **deconvolution** on planetary features, we have modeled the effects of this procedure on an artificially generated planetary image which has sharp limbs and a sharp **albedo** feature such as a polar cap. The image of the planet, to which suitable noise was added, was convolved with a PSF function using Fourier transforms to emulate a raw HST image. This was then deconvolved using the same PSF function using the Richardson-Lucy algorithm. Figure 4 shows intensity scans across the images for a) the input image, b) the raw "**HST**" image, and c) the deconvolved image. At least for this simple case, the true limbs of the planet are located at about 15% maximum intensity; the true edge of the polar cap defines the intensity midpoint in the deconvolved **image**, as might be intuitively guessed. The deconvolved image also preserves the intensity levels found in the true image. This numerical experiment serves as a guide for locating limbs and polar cap boundaries.

4. Atmospheric and Polar Phenomena

The observations of Mars acquired as part of this series spanned late northern winter and spring on Mars, $L_s=348$ and $L_s=60$. The images of the Syrtis Major face are shown at their correct relative size in Figure 1. Historically, the season around the vernal equinox has been transitional in terms of its meteorology. The classic duststorm season has ended when these observations commence, and the discrete, white clouds of northern late spring and summer have just appeared when the observations end (Smith and Smith, 1972). The north polar cap begins to sublime, and the initial condensate deposits are observed in the south. The north polar hood dominates through the first half of this period, after which it disappears to reveal the surface polar cap. The existence of a southern hood to rival that in the north has been disputed; if it were to follow the same seasonal cycle as the north hood, it should appear during this period.

As expected, the north polar hood does dominate the violet (413M) images acquired in December, January, and February. The edge of the hood on the central meridian ranged between 45 and 53 degrees north latitude in all of these images. There was a consistent tendency in all four violet images for the hood to be skewed with a more southward extent in the western (a.m.) part of the hood and a more northerly boundary on the afternoon portion of the hood. This observation suggests an increase in the extent of the hood during the night. As has been noted by terrestrial observers for many years, the hood is much more prominent in blue and ultraviolet wavelengths than in longer, red wavelengths. 673N images acquired during the same sequences clearly reveal dark albedo features in regions where blue images show the presence of the hood. Nor is there any clear indication of a surface cap in the red images. However, the north pole was tilted away from earth during all of these observations so that the region within 65 degrees latitude was visible only at the very limb; and, in fact, some of the red images do reveal weak brightening at the northernmost edge of the planet which could be due to the surface cap.

The violet and W images in the third December sequence, in which the longitude of the central meridian is 61 degrees for the 413M image, reveals the especially interesting structure in the north polar hood shown in Figure 5. The "peninsular" extension of the hood extending roughly 2200 km from Tempe past Alba Patera is possibly the visible manifestation of a front such as those which were observed extensively during the Mariner 9 mission (Briggs and Leovy, 1974). Inasmuch as this was the only view of this particular region when the hood was extant, we cannot rule out, on the basis of these data, the possibility that this phenomenon is more permanent. In the January image, there is a small extension of the hood into the northern part of Arabia which is also visible, to a lesser extent, in the December image of the area. The

December **image** centered at 61 degrees is also interesting because it strongly suggests an annular structure of the hood: that is, an **annulus** of bright clouds surrounds a darker core. Hood observations on Mariner 9 also suggested that the interior of the hood is much more diffuse than the outer portions (**Briggs and Leovy, 1974**). This annular structure seems to be unique to the third December image, however, possibly implying an asymmetry in the hood relative to the geographic pole or temporal variability on a relatively short **timescale**.

In addition to the north polar hood, the images also reveal some clouds in the mid-latitudes of the southern hemisphere. In the December and January images of the Syrtis region, clouds were observed stretching from the morning terminator to the **Hellas** basin; these relatively thin clouds were similar in the two images though more pronounced in December. A similar cloud stretching from the morning limb to Argyre was seen in the third December sequence. A more substantial southern hemisphere cloud was seen in the February violet image covering only the western portion of the **Hellas** basin; this cloud was not visible in the red images suggesting that it was composed of a condensate.

The afternoon limbs are bright in both red and blue in January and February. Because the central meridians differ by 15 degrees between the two images it is likely that the limb brightening reflect general atmospheric aerosols rather than a cloud associated with a particular geographic area, such as **Elysium**. There are also brightening along the south limb of the planet in the blue images which should not, however, be confused with a south polar hood. These brightening are weak despite the fact that the southerly sub-earth latitude in these images would favor observation of a south hood, if it existed.

In the May images, on the other hand, the north pole is tilted towards earth; and all three **413nm** images acquired then show substantial brightening in southerly latitudes which does strongly suggest a south polar hood has formed by $L_s = 60$ degrees. This season is the most difficult to observe from earth, since Mars is near perihelion; and the south polar region is tilted away from earth. However, examination of photographic images from many relevant oppositions shows that a south polar hood is common during mid to late southern fall (Martin, private communication). The HST images confirm the south **hood's** existence during this season.

The three sequences of images acquired in May, 1991, at $L_s = 60$, are rich in equatorial and mid-latitude cloud structure. In order of acquisition, the 413M images have central meridians of 283, 43, and 161 degrees respectively. The geometry is such that the historically cloudy areas of the martian northern hemisphere, the Tharsis/ Vane's Marineris region, **Elysium**, and Arabia will appear near the morning terminator and/or afternoon limb in one or another

image. Clouds were seen in all of these regions; the photometric angles and intensities for these are summarized in Table III. The three violet May images are shown in Figure 6.

The **Tharsis / Vanes Marineris** region was observed in both the morning and in the afternoon, providing an opportunity to observe the growth of significant clouds in the region. The region of **Tharsis, Olympus Mons, Alba Patera**, and the western branches of Vanes Marineris has long been known for the "W" clouds, so named by Earl Slipher (1962), which are prominent there from mid northern spring to mid-summer. Contrary to popular opinion, Olympus and the large **Tharsis** volcanoes are not necessarily the principal parts of the cloud complex, which is actually variable from year to year and from time to time within the "cloud season." In the morning views of this region there are two well developed clouds: over the northern flanks of Alba Patera and **Tithonius**, the region to the north of **Noctis Labyrinthus**. These clouds are very prominent in the afternoon view of the region, and a significant, but more optically thin, component is seen to the west of **Ascraeus Mons**. Only a very dim cloud is seen over Olympus Mons in the afternoon view; however, Olympus is farther from the limb so that the cloud is not so enhanced by emission angle effects as the others. A contour plot of this region is shown in Figure 7.

The most prominent cloud observed during northern spring is the afternoon cloud associated with the **Elysium** region. It is somewhat brighter than the Tithonius cloud despite the fact that it is at a significantly smaller emission angle. As will be discussed in the next section, an optical depth of 0.4 is estimated for this cloud using ultraviolet images. The **Elysium** cloud is also geographically the largest, with at least some associated haze 22 degrees to the west of the principal cloud. The **Elysium** cloud is less obvious near the morning terminator than those in the **Tharsis** region. This is not likely to be due to illumination since it is no closer to the terminator than the Alba cloud; Hunt et al. (1980) observed on Viking images that the **Elysium** cloud was quite diffuse in the early morning, consistent with these observations. The cloud over Arabia, while certainly evident on the relevant images, is not as bright at 413 nm as are the clouds over **Alba, Tithonius, or Elysium**.

Clouds in the **Elysium** region are well documented historically (Smith and Smith, 1972; Hunt et al., 1980; Martin and Baum, 1969); the clouds have been observed to be very stable in position relative to **Elysium** during the seasons in which they occur and **interannually**. Images at 413, 502, and 673 nm are available for the **Elysium** cloud. These images were used to construct a color composite. The color of the **Elysium** cloud was white, indistinguishable from the north polar cap, rather than blue, as the north polar hood, or yellow, as expected for dust. The **Elysium** region is a permanent bright **albedo** feature in addition to being a location of well documented cloud activity; such bright regions are

thought to be mantled with deposits of dust, so it is of interest to consider the possibility of a dust component in this cloud. Martin and Zurek (1993) report historical observations of local dust activity in the **Elysium** region though it has never been the site of regional dust activity.

A detailed consideration of the shapes and locations of the intensity **isolines** of the **Elysium** cloud reveals differences between the cloud configurations mapped in red, green, and blue. The cloud image at 413 nm is displaced towards the limb relative to the 673 nm observation; this can be explained by a significant Rayleigh component to the cloud brightness which would lead to an increase in the red/blue ratio as the emission angle (and optical depth) increases. The shape of the contours varies between the three colors, and the cloud appears to be more diffuse in both red and blue than in green. These observations could be interpreted in terms of some localized, spatially variable dust component in the cloud, although variations in the large surface contribution to the overall red brightness could also explain the results. Differences are also observed between the red and blue contours for the other May clouds, especially for the Arabia cloud which is also in a classic bright region thought to be a sink for dust. Although there is substantial variation in brightness between the clouds at 413 nm, the intensities are more nearly equal at 673 nm. Analysis of the W observations, to be discussed in the next section, suggests that not much dust is present globally; however, those results are based on limb brightening and could miss local dust contributions.

The best case for dust activity during our observations is near the afternoon limb at the edge of the north polar cap; the extent of the cap towards the pm limb on the three red May images is clearly greater than on their blue counterparts. The similarity of the three images suggests a dusty atmosphere near the cap edge in afternoon, possibly reflecting dust entrained with subliming CO₂, rather than a bright surface feature.

As noted previously, the March and May images clearly show the north polar cap during its spring recession phase; the north pole is tilting towards earth during this time, improving the view of the cap. There have been many observations of this phenomenon during this season, both by terrestrial astronomers and by Viking and Mariner 9 spacecraft; it is therefore interesting to compare the 1991 HST observations with these other data sets from prior years. **Blue** images which show a surface cap consistently reveal a larger extent of the cap on the morning terminator than do the red images, suggesting morning condensate clouds near the cap edge. As noted above, there are similar suggestions of possible dust near the afternoon limb.

There are several sources of error in making measurements of the

polar cap boundary, **Two** such problems are determining the precise boundary on **the** images and finding **the** center (sub-earth point) on the images; the reduction to latitudes and longitudes is tied to determination of the sub earth point. In principal, our analysis of the effects of spherical aberration and **deconvolution** with the Richardson-Lucy routine makes it possible to define a prescription for locating the cap edge on an image. The analysis discussed there would be suitable for a case of a constant **albedo** Lambertian cap superposed on a constant **albedo**, Lambertian surface. The real cap, however, will not appear as a simple step function, as assumed in that calculation, because of a lack of sharpness in the edge, non-uniform **albedo**, and non-Lambertian phase function. We have estimated this effect as a ± 0.5 pixel error in locating the edge. Also, the exact sub-earth point on the planet's disc is needed to map from pixel space to latitudes and longitudes on the planet; this is particularly important near the limbs of the planet and therefore has a large effect in the polar regions. Since the limbs are not sharp and because the phase is large for the images which were used to measure caps, we feel that we can at best locate the center within a 0.5×0.5 pixel region. These two sources of error produce an uncertainty of ± 1.5 degrees in the edge of the cap.

An additional source of systematic error results from an uncertainty in the scale of the Planetary Camera images. The WFPC Science Verification report list values for the scale ranging from .0437 arcsec/px to .0444 arcsec/px (**WFPC Team**, 1991) . This range in scale produces **an** additional uncertainty in latitude of $\pm 1.2^\circ$ at the edge of the cap; we adopted a scale of 0.044 **arcsec/px**, near the mean of these various determinations.

Using the analysis described above to determine the cap edge, latitudes of 70.9 degrees, 69.7 degrees, and 71.8 degrees were determined at central meridians of 161, 283, and 43 degrees respectively for the L, = 60 images (these measurements, by PBJ, made use of the 413M images; **LJM**, using the 502N image at ≈ 283 LCM, deduced a cap edge latitude of 70 degrees). The mean value of 70.8 degrees is very close to previous spacecraft and observational data reported by James (1979,1980) and **Iwasaki** et al. (1979,1992); the cap latitude for the 1979-80 regression at L, = 60 is 70.7 degrees according to the empirical fit to the Viking data (James, 1982) . Although the cap is not expected to be perfectly circular, the potential uncertainties in the measurements preclude any conclusions regarding azimuthal variation in the cap radius. The cap edge measured on the 413M image was at 65.8° for the March image, L, = **35**, which is also in agreement with the value of 65.3° on the basis of the empirical linear regression fit. The measured cap edge on the March 673N image is 66° ; no essential difference between images using different filters is observed.

There seems to be no evidence in these data for any deviation of the north cap regression from its normal pattern during mid-spring

in 1991. While there are historical indications of interannual variability from the (superior) earth based observations of the retreat of the south polar cap (James and Martin, 1987), all observations of the recession of the north cap during the period of interest here are consistent with it being quite repeatable and independent of dust storm history except for the 1960's data reported by Capen and Capen (1970). The behavior of the cap in mid-spring in the two Viking years, which had very different dust histories, were quite similar (James, 1980). Therefore, the 1991 HST observations are consistent with a repetitious recession for the north polar cap.

5. Ultraviolet Imaging of Mars

HST provides a unique opportunity to obtain high spatial resolution at ultraviolet wavelengths in both imaging and spectroscopic modes. For Mars observations, this capability is particularly well suited to measurements of Rayleigh and cloud scattering and atmospheric dust and ozone absorption. As part of the ongoing Mars monitoring program with HST, we obtained several **WF/PC** images and Faint Object Spectrograph (**FOS**) spectra of Mars over the 220-340 nm wavelength range during the six months following the 1990 opposition of Mars. This spectral region incorporates the Hartley ozone absorption band, which we have used to map ozone in the atmosphere of Mars. More than 70% of the observed reflectance of Mars at 220 nm is due to Rayleigh scattering by the CO₂ atmosphere, apart from variable cloud and polar cap reflectance, because the surface reflectance of Mars is less than .02 at these ultraviolet wavelengths (Herd et al., 1974). As the Rayleigh scattering cross section decreases by a **factor-of-five** between 220 and 320 nm, the HST ultraviolet measurements provide a very sensitive measure of Mars atmosphere dust, ozone, and cloud opacities relative to the well-known Rayleigh scattering opacities of the Mars atmosphere.

In the following, we present an analysis of **WF/PC** images of Mars obtained using the 230W and 336W filters, for the periods December 13, 1990 and May 15, 1991. The 230W and 336W filters were chosen to obtain images of Mars within and outside the Hartley band (see Figure 8). As a consequence, ratio images of the 230W/336W image pairs provide a uniquely global view of Mars atmospheric ozone at good spatial resolution, even when the angular diameter of Mars falls below 5". The angular resolution achieved upon **deconvolution** of the HST uv images (as described in the previous sections) is approximately 0.2". FOS scans across Mars were also obtained in January and February of 1991; they are presented in a separate paper (Clancy et al., 1993). These data consist of calibrated reflectance spectra of Mars over the 220-230 nm wavelength region, obtained with ≈ 2 nm wavelength resolution within two parallel .25" apertures which scanned the planet. The

results derived from the **WF/PC** ultraviolet imaging are consistent with the **results** Of the FOS data analysis, particularly **regarding** the Mars **surface albedo** between 220 and 330 nm, which is better constrained by the FOS data.

The December 1990 and May 1991 ultraviolet images of Mars are shown in Figure 9. The **deconvolved** 230W and 336W images as well as the ratio 230W/336W image are presented for both periods. Key observational aspects of Mars corresponding to these observations are provided in Table IV. Notice that the Mars season (L_s) and angular diameter changed from 340° and 16.5" in December 1990, to 60° and 4.9" in May 1991. High southern latitudes are visible in the December 1990 images (**Lat_{SE}** = 12°S) , whereas high northern latitudes are more prominent in the May 1991 images (**Lat_{SE}** = 12°N) . The central meridians of Mars corresponding to both observations *cross* the Syrtis Major region. The local time of the central meridian for the May 1991 image is distinctly earlier in the morning compared to the December 1990 observations (see table IV) .

The 230W images were obtained with 200 second integrations; the 336W images required much shorter 1 second integrations to achieve comparable signal levels of 100-500 counts per pixel on the disk of Mars. The absolute calibration of these uv images, $\approx \pm 30\%$, is based on internal calibration of the WF/PC; as described earlier, we did not obtain a good external calibration for these images. Instead, we adjusted the calibration of the center of the images to agree with model reflectance (see below), which incorporate Rayleigh scattering opacities and uv surface **albedos** from the FOS observations (**Clancy et al.**, 1993) and previous Mariner 9 ultraviolet observations (**Herd et al.**, 1974). As discussed below, our analysis of these uv images is based primarily on the center-to-limb variations in brightness and the differences between the 230W and 336W images.

A more significant issue regarding the analysis of these HST uv images is an observed red light leak in the uv filters (**MacKenty et al.**, 1992). Prior to launch this red leak was estimated to contribute $\leq 2\%$ flux to 230W images of a **KOIII** object (**MacKenty et al.**, 1992), which would suggest a comparable red leak contamination for 230W images of Mars. Such a level of red light contamination would not be discernible or important in our analysis of these images. However, there also exists a time-dependent degradation in the throughput of the HST camera due to the buildup of uv absorbing contaminants on the camera optical system (**MacKenty et al.**, 1992). This effect is most important for the 230W images, where the contamination due to the red leak approaches 100% as the uv throughput of the system decreases to essentially zero over a 2 month period. One method for removing this contaminate from the HST camera is to allow the camera temperature to rise above 10° C, which essentially sublimates the uv contaminant from the camera optics. Such warming occurs during **safings** of the HST spacecraft;

fortuitously, such events occurred shortly before both the December 1990 and the May 1991 observations of Mars. The observed count rates in both cases for Mars indicate modest uv sensitivity loss ($\leq 20\%$) at the times of our observations, consistent with **small** ($\leq 10\%$) red leak contamination to our Mars uv images. In addition, comparisons to the FOS observations and the results of the analysis presented below are inconsistent with significant red leak contamination of our Mars uv images.

The 230W and 336W images of Mars in Figure 9 display a variety of surface and atmospheric phenomena which were discussed in the previous section using the violet filter images. For example, the bright regions apparent in both filters at high northern latitudes indicate the presence of the late-winter polar hood in the December image and the seasonal surface cap in May. The distinct darkening in both 230W images at the north polar limbs indicates ozone absorption. This absorption is more striking in the 230W/336W ratio images for both periods; the ratio image also suggests significant ozone absorption at southern high latitudes as well. Strong Rayleigh scattering in the 230W images can be seen in the enhanced limb brightening evident on the illuminated evening limb (right side of images) and over the deep **Hellas** basin, which appears in the lower right portions of the December 1990 230W and 230W/336 images. Clouds are also evident in the morning southern mid-latitudes in the December 1990 image and over **Elysium** Mons on the evening limb of the May 1991 336W image. A detailed analysis of these images in terms of atmospheric ozone columns, cloud opacities, and dust opacities is presented below.

6. Radiative Transfer Modeling

We constructed a radiative transfer model of multiple scattering and absorption by the molecular atmosphere (**Rayleigh**), clouds, dust, and ozone. This model employs the discrete-ordinate code of Stamnes et al. (1988) and a lower boundary surface with specified **albedo**. For the purpose of specifying the vertical distributions of Rayleigh and cloud scattering versus ozone absorption, we used three levels corresponding to altitude ranges of 0-10, 10-20, and 20-50 km. Rayleigh, cloud and dust opacities for each layer are calculated assuming a 10 km scale height of vertical mixing. The vertical distribution for ozone opacity is derived from the latitude dependent photochemical model of Kong and McElroy (1977), and ozone absorption cross sections are taken from DeMore et al. (1990). The total **Rayleigh** opacity [1.3 at 225 nm, .032 at 320 nm for 0 km altitude] is derived from the surface pressure observations of Viking (Hess et al., 1977), USGS surface altitude maps of Mars, and **Rayleigh CO₂** cross sections from Allen (1973). The cloud and dust scattering phase functions are adopted from the Viking IRTM emission-phase-function (**EPF**) analysis of Clancy and Lee (1991). HST observations are primarily sensitive to

backward scattering, i.e. near 180° scattering angle, since all Mars observations were at phase angles less than 30° . The Viking EPF analysis obtained the best constraints for the backscattering cross sections of dust and clouds. Cloud single scattering albedos are assumed to be 1.0, appropriate to pure H_2O or CO_2 ice at the observed wavelengths. Dust single scattering albedos are assumed to be 0.4-0.6, based on Mariner 9 UVS observations during the 1971 global dust storm (Pang and Ajello, 1977). In our modeling of dust and cloud scattering, we assume both aerosols to be vertically distributed with a constant mixing ratio to the atmosphere density.

We specify the surface albedo of Mars to vary between .01 at 220 nm, to .02 at 330 nm. This compares to an albedo of .0156 at 305 nm, derived from an analysis of Mariner 9 WS observations by Herd et al. (1974). The wavelength dependence of the ultraviolet surface albedo adopted for our analysis of the HST uv images is based on analysis of the HST FOS observations of Mars (Clancy et al., 1993). In fact, however, the results of our analysis of the HST UV images analysis do not change significantly when a wavelength independent-albedo of .015 is assumed. We also specify that the uv surface reflectance of Mars varies with incidence angle in a manner consistent with a Minneart limb darkening coefficient of 0.7. The observed limb brightening of Mars at 220-330 nm is primarily controlled by Rayleigh scattering and, near the poles, by cloud scattering. The specified surface limb darkening serves to reduce the calculated limb brightening by $\approx 20\%$ at 336 nm but by only $\approx 5\%$ at 220nm. For the case of the May 1991 images, we derive uv Lambert albedos of .10-.15 between 220 and 330 nm for the north polar seasonal cap, as discussed below.

For the purpose of comparing model and observed uv reflectivities of Mars, we used east-west and north-south cross sections from the 230W and 336W HST images of Mars. These cross sections provide a representative analysis of cloud, dust and ozone opacities in the Mars atmosphere, as well as latitudinal gradients in the cloud, ozone, and surface ice distributions. For all of these comparisons, we scaled the observed Mars reflectance at the center of the disk to agree with the model reflectance. The required scale factors are consistent with 20-30% calibration errors in the observations, which fall within the estimated uncertainties of the image calibrations. Our analysis is primarily sensitive to the center-to-limb reflectance variation of Mars, rather than the absolute reflectance. The north and south limbs reflectance are large relative to the disk center due to Rayleigh scattering and to the polar hood (December 1990) or surface ice (May 1991) at high latitudes (cf., Figure 9). Atmospheric ozone, which strongly affects the ratio of limb brightening between the 230W and 336W images, is also concentrated at polar latitudes (Barth et al. 1973). The fully illuminated east, or afternoon, limb at equatorial latitudes is brightened relative to the disk center due mainly to Rayleigh scattering. For the December 1990

image, which exhibits the highest spatial resolution with minimal cloud scattering at low latitudes, the observed limb brightening on the east limb provides the most sensitive measure of atmospheric dust loading at the time of the observations. Small amounts of dust will reduce limb brightening in the 230W images in particular.

Figure 10 presents the results of calculations of reflectance along the central meridian of the December image ($\approx 300^\circ$ W, in Syrtis). The heavy solid-line indicates results which include the model surface **albedo** and limb darkening, Rayleigh scattering accounting for elevations, and a polar hood of optical depth ≈ 0.2 . The heavy dashed-line presents the best fit including ozone absorption at high latitudes; meridional distributions of ozone column abundance and polar hood opacity are presented in Table Va. **Hellas** basin is evident in the 230W cross section by the increased brightening near pixel 160 contributed by the enhanced Rayleigh optical depth over this deep basin. The north polar hood (pixels 400-450) leads to roughly equal brightening of the north limb of Mars in the 230W and 336W scans. Rayleigh scattering, however, increases the limb brightening in the 230W cross section relative to the 336W cross section; this effect is most evident near the southern limb (and in the east/west cross sections), where the polar hood is absent. The morning clouds evident in the southern hemisphere in Figure 9 are not sampled by the cross section presented in Figure 10. The uv opacity of this cloud peaks at around 0.05, as indicated in Table Va. The model ozone columns in the northern and southern high latitude regions lead to substantial reduction in the polar limb brightening for the 230W observations, without discernible impact on the 336W observations. As indicated in Figure 8, the ozone absorption is smaller by between one and two orders-of-magnitude in the 336W versus the 230W images.

East/west scans across the December, 1990 images are presented in Figures 11a and 11b for the 230W and 336W filters, respectively. These cross sections correspond to latitudes of 0-10S on Mars. The solid-line model curves represent pure Rayleigh scattering by the martian atmosphere and reproduce the limb brightening observed in the 230W and 336W images. In contrast, small amounts of dust ($\tau = .20$) or ozone (column = 4 $\mu\text{m-atm}$) reduce the limb brightening in the 230W images, as indicated respectively by the dashed and dotted-line model profiles presented in Figures 11a. In fact, atmospheric dust loading produces overall reduced reflectance for Mars at both wavelengths. However, we have normalized all of the models to agree with the observed reflectance at the center of Mars. The smaller backscattering cross section and ultraviolet single scattering **albedos** (0.4-0.6) of dust relative to Rayleigh scattering are the key reasons atmospheric dust leads to a reduced reflectance of the Mars atmosphere/surface at the small phase angles of these observations. We conclude that atmosphere dust opacities were less than 0.1 and that low latitude ozone abundances were less than 4 $\mu\text{m-atm}$ at the time of the December 1991

observations. Stronger constraints on low latitude ozone are possible from the FOS data (Clancy et al., 1993). We also point out that a significant red leak in the 230W filter is inconsistent with the limb brightening observed in the 230W image. A 30% red light contribution to the 230W image would reduce the 230W limb brightening to one-half of its observed value.

North/south cross sections from the May 1991 uv images, shown in Figure 12, sample longitudes crossing the eastern margin of Syrtis. In May, at $L_p = 60$, the north polar surface ice cap is exposed, and the polar hood has dissipated. The heavy solid-line profiles show model results for Rayleigh scattering with a north polar ice cap and weak clouds ($\tau = 0.1$) over southern high latitudes. The ice cap was modelled with a Lambert albedo varying with latitude and wavelength as tabulated in Table VI. The heavy dashed-line profiles represent models which include ozone absorption at polar latitudes. The May 1991 images also reveal significant cloud opacities over the high Arabia region which correspond to the clouds observed in the violet images which were discussed previously. The enhanced uv reflectance over Arabia are consistent with cloud opacities ≈ 0.2 , as indicated by the dotted-line model profiles in Figure 12. The derived meridional distribution of ozone is included in Table Vb, as well as the relevant cloud opacities. The north seasonal ice cap albedo versus latitude is presented in Table VI along with the model albedo for the surface of Mars.

The Elysium region is on the afternoon limb of Mars in May, and the prominent Elysium cloud discussed in the analysis of the violet images is clearly evident in the uv images in Figure 9. Figures 13a and 13b present 230W and 336W reflectance cross sections from southern low latitudes ($\approx 10^\circ\text{S}$) across the morning terminator to Elysium (25°N), which is near the fully illuminated afternoon limb. The solid-line model profiles incorporate 40% reduced Rayleigh opacities due to elevation over the Elysium region and a peak cloud opacity of 0.4. The darkening in the May 1991 ratio image over Elysium does not require ozone absorption, although the occurrence of a blemish in the 230W image coincident with the brightest part of the Elysium cloud leaves some uncertainty with this conclusion. The reduction in 230 nm brightness relative to 336 nm brightness over Elysium can be attributed to reduced Rayleigh scattering over the high Elysium region. The Elysium cloud opacity is the largest associated with any clouds observed in HST 230W and 336W images. Southern low latitudes exhibit minimal cloud scattering (Figure 9), allowing determination of possible dust absorption. However, reduced spatial resolution in May relative to the December images allows less stringent constraints on dust absorption. We find that the dust opacity for the May 14, 1991 period was less than 0.2 for southern low-to-mid latitudes.

A synthesis of the HST Ultraviolet imaging analysis is provided in Tables V and VI. Uncertainties in the cloud opacity and column abundance calculations are estimated to be 20%, due primarily to assumptions in the modeling analysis. The inferred cloud opacities, ranging from 0.1 to 0.4, compare reasonably well with the Viking EPF derived solar band opacities of clouds (Clancy and Lee, 1991) for fall mid-latitudes and polar latitudes. The HST ultraviolet cloud opacities over the Arabia and Elysium regions also compare favorably to similar cloud opacities derived from Phobos KRFM ultraviolet observations in 1989 (Moroz et al., 1991). The HST measurements of polar ozone are generally consistent with the Mariner 9 UVS measurements in 1971-1972. Mariner 9 observations for the same seasons present ozone columns of 5-20 $\mu\text{m-atm}$ for northern and southern high latitudes (Barth et al., 1973). With respect to seasonal changes in ozone abundance, there was a significant decrease in ozone concentration in northern high latitudes between $L_s = 344$ and 59 and an increase over high southern latitudes; for example, the ozone column abundance decreased by roughly a factor of two at 60°N between $L_s = 344$ and 59 and increased by a similar amount at 60°S during the same time period. This is qualitatively consistent, via the anticipated anti-correlation between ozone and water vapor, with the seasonal variation in water vapor anticipated on the basis of Viking results.

The HST images do not place stringent limits on low latitude ozone columns. However, HST FOS measurements allow much stronger constraints on low latitude ozone as well as ultraviolet surface albedos (Clancy et al., 1993). The HST ultraviolet images indicate that the seasonable ice cap of Mars, observed at an L_s of 59° in May 1990, exhibits an albedo roughly ten times the typical surface ultraviolet albedo of Mars. However, this albedo is still far below that exhibited by clean ice. On the other hand, the ultraviolet limb brightening of Mars at low latitudes indicates a generally dust free atmosphere for both seasons in which Mars was observed.

7. Observations of Variable Albedo Features

Variability of classical albedo features on Mars has long been noted by terrestrial observers (Slipher, 1962; DeMottioni, 1975). Spacecraft observations of such features have shown that the variability is related to aeolian transport of bright dust into and out of the regions, primarily in association with major dust storm activity (cf. Sagan et al, 1973; Thomas and Veverka, 1979). Studies of the amount and direction of this dust transport reveals regions which at present act as either sources (net erosion of dust from an area) or sinks (net deposition of dust in an area) of dust (Lee et al, 1982; Christensen, 1988).

Ground-based observations can adequately monitor Mars for only the relatively **small** portion of the martian year when the planet is near opposition. Temporal observations covering all martian seasons therefore require about fifteen Earth years, making it very difficult to distinguish episodic variability from seasonal or interannual variability. Orbiting spacecraft, such as the Viking Orbiters, have provided observations spanning slightly more than two consecutive martian years but have not provided the synoptic coverage desirable for monitoring regional **albedo**. Observations from HST are limited only by the fifty degree solar exclusion angle and scheduling priorities, allowing repetitive coverage over more than half of the martian year.

HST's spatial resolution and broad spectral capabilities make it a very useful platform for synoptic observations of variable **albedo** features. Due to limitations in the number of exposures which could be scheduled on HST, we adopted the strategy of concentrating synoptic observations on the Syrtis Major region of the planet which is one of the principal areas showing large **albedo** variations. We shall first review Viking Orbiter observations of the Syrtis Major region, and we shall then compare these to our Cycle 0 HST observations

Historically, Syrtis **Major** is one of the most distinct and variable of the classical dark **albedo** features on Mars, with seasonal / interannual variations in its size and **albedo** readily evident to terrestrial observers (Slipher, 1962). Spacecraft observations have shown that the feature is composed of numerous westward-trending bright and dark wind streaks (Sagan et al, 1973) and dune fields (Simpson et al, 1982) lying on the generally **low-albedo** slopes of a volcanic shield (Schaber, 1982). Therms 1 inertias, derived from Viking Infrared Thermal Mapper (IRTM) observations, of about $8 \times 10^{-3} \text{ cal/cm}^2/\text{sec}^5/\text{K}$ also **suggest** a sandy surface (Kieffer et al, 1977; Jakosky, 1986).

During the first **martian** year of the Viking missions, two global dust storms occurred. Plots of the optical depth as a function of **L**, observed by the Viking Lander in **Chryse** Basin (Figure 14) clearly show these storms. Orbiter images revealed dramatic changes in the Syrtis region following the end of the second storm. Figure 15 shows two views of the area, the first obtained at $L_s = 350$, about one eighth of a martian year after clearing of the second storm, and the second obtained at $L_s = 77$, about one quarter of a martian year later. Changes in the Syrtis region during this time period are evident: the dark **albedo** feature has effectively expanded in area during this time.

Albedo variations on Mars were determined quantitatively using the broad band visual channel on the IRTM instrument; these detectors covered the spectral range from 0.3 - 3.0 μm (Kieffer et al., 1977), providing a broad-band albedo measurement calibrated to 1-2%

(Pleskot and Miner, 1981). Mapping sequences provided systematic observations of **large** areas of the planet throughout much of the Viking missions; Figure 16 is an example of one such sequence covering the Syrtis Major region. The viewing geometry and surface location are determined for each observation, allowing the visual brightness values to be converted to Lambert **albedo**. For the purposes of temporal and spatial mapping of Syrtis Major, observations obtained over a restricted time interval (typically less than an hour) were binned to a spatial resolution of 2.5 x 2.5 degrees. The maps generated in this fashion have been displayed as images for direct comparison to HST images.

Figure 17 shows a series of Lambert **albedo** maps of Syrtis Major spanning the martian years preceding and following the two global-scale dust storms observed by Viking. The plot of atmospheric opacity as a function of time in Figure 14 clearly shows the timing of these IRTM observations in relation to the dust storms. Dramatic temporal variability in the regional **albedo** is evident in these maps. The central portion of the feature darkens slightly preceding the first dust storm (note the changes between Ls = 172 and 198). The region exhibits a general increase in **albedo** following the first storm and again after the clearing of the second storm (note the changes between Ls 198, 259, and 356). A general decrease in **albedo** is apparent in the subsequent time steps (compare the maps for Ls 356, 32, and 134), until the region has essentially returned to its pre-storm appearance. Such behavior is consistent with the earlier studies of Christensen (1988). The area exhibiting the largest **albedo** variation (near 10 degrees latitude, 290 degrees longitude) is associated with the dune-covered area near the crest of the volcanic shield; the Lambert **albedos** for this area range from a minimum of about 0.10 at Ls = 198 to a maximum of about 0.20 at Ls = 259 back to a minimum of about 0.08 at Ls = 134.

The observed variability in regional **albedo** is consistent with the presence of the active aeolian environment at the time of Viking. The observed wind streaks trend to the west, consistent with the **Hadley** circulation expected throughout the year at these latitudes (Kahn, 1983). The presence of dunes, numerous intracrater splotches and deflationary wind streaks, and the relatively high regional thermal inertia are all indicative of a surface covered with sand-sized particles. Following global dust storms, enhanced deposition from the atmospheric dust load increases the regional **albedo**. Subsequently, the sandy surface is driven to **saltation** by the effective regional winds, readily ejecting the deposited bright dust into suspension. Net removal of dust from the region results in a decreased regional **albedo** as the year progresses. This process would presumably be repeated in any such dust storm cycle: enhanced deposition and increasing **albedo** after the storm events are followed by ejection of dust from the mobile surface and decreasing **albedo**.

The first **cycle** of HST observations of Mars provides an opportunity to compare the **current** appearance of the **Syrtis Major** region with that at the time of Viking, more than a decade earlier. As described previously, Cycle 0 images were obtained for five times beginning at $L_s = 349$ and ending at $L_s = 59$, a time span of about one-sixth of a martian year. Figure 1 includes the sequence of images obtained using WF/PC and the F673N filter; each image was deconvolved using synthetic point-spread functions (generated for the appropriate location of the planet's center on the **CCD**) and sixty iterations of the Lucy-Richardson algorithm. The varying size and phase of Mars is apparent in this figure. To a first order, the Syrtis Major feature appears unchanged over the time of these observations; clearly there are no variations of the sort observed by Viking during a similar martian season following the 1977 dust storms.

The individual images were map-projected to facilitate comparisons of features on different images. Figure 18 depicts the **Syrtis Major** region using the same projection and scale as the **IRTM albedo** maps discussed in the previous section. Note that we have not attempted to compensate for the effects of varying lighting and viewing geometry in these maps. However, other than the variability in the southwest corner of the maps (due to the changing phase of the planet) and effects due to changing resolution, the appearance of **Syrtis Major** is essentially unchanged over this time period.

The stability of **Syrtis Major** from late-1990 through mid-1991 is consistent with the scenario outlined for the Viking observations only if no global dust storm occurred during the usual dust storm season prior to these observations; in this case there would be no period of enhanced dust deposition followed by dust erosion in the region. Dust storms are the essential ingredient in the cycle of dust deposition and erosion thought to underlie the **albedo** variability of this region. Once most of the dust has been transported from the region, significant variability will not occur until a dust storm again initiates the cycle.

Hellas basin is also visible in this series of images to the south of Syrtis Major, though with much less favorable viewing geometry. Several features which have been reported by telescopic observers are clearly visible in the December 673N image. The west rim of **Hellas**, classically called **Yoanis Fretum**, is unusually evident in the image as a dark arc terminating in the dark spot **Nerei Depressio** which, on the basis of current topographic knowledge, is actually an elevated area rather than a basin. The bright wedge between **Yoanis Fretum** and the Mare Serpentis / **Hellespontus** region is **Yoanis Regio**. Connecting to the diffuse dark blob near the center of **Hellas**, **Zea Lacus**, are two streaks previously identified with canals: northward trending **Alphens** and eastward trending **Peneus**. Finally, the dark east-west arc which runs from near **Nerei Depressio** towards **Eridiana** is a feature which is not clearly

identified on **Slipher's** (1962) map. These dark **albedo** markings in **Hellas** continue the darkening trend clearly seen during the 1980's in **Solis Lacus** and other Southern Hemisphere areas. Again, changes in brightness may be interpreted in terms of surface dust cover. If so, 1990 was not a very dusty year in **Hellas**.

The HST observations discussed here span only a fraction of a martian year. Future analyses will include observations obtained during HST Cycle 2; these will significantly overlap the same season viewed during Cycle 0 but will expand the temporal coverage of the HST database to two martian years. If a global-scale dust storm occurs in the interim, subsequent HST observations will provide a valid test of the Viking-era "**cyclic** dust deposition and erosion" hypothesis.

8. Conclusions

Most of the evidence accumulated by HST on the martian surface and atmosphere are consistent with a Mars which is quite different from the planet when it was viewed by Viking. The atmosphere throughout the observation period was rather clear, and no compelling evidence for dust activity except near the receding north polar cap was found. In addition, the surface behavior in the **Syrtis** Major region is consistent with the absence of major dust activity during the preceding southern summer. Low dust activity is also consistent with observations of Mars during the 1986 and 1988 oppositions; particularly in the former, there was little evidence for dust activity (James et al., 1990) and the atmosphere was cold, suggestive of small dust optical depth (**Clancy** et al., 1990). Taken as a group, these observations indicate that the years of intense dust activity in the 1970's has given way to a clear, relatively dust-free planet in the late 1980's and early 1990's.

This different climatic regime does not seem to have had appreciable effect "on some aspects of the surface and atmosphere which one might expect to correlate with changes in atmospheric aerosols. Within the error limits described above, the behavior of the north polar cap seems to have been similar to that during the Viking years despite the relatively large effects that the global storms seemed to have on the polar atmosphere in 1977 (**Jakosky** and **Martin**, 1987). Since there was not a large difference in the behavior of the north cap between the two Viking springs in which it was observed, so this may not be a dependable indicator of dust activity. Observations of clouds showed no radical departure from earlier observations: a prominent north polar hood in late winter, thin morning clouds in the antarctic region during the same season, development of a south polar hood during mid-autumn, and discrete clouds in mid-spring in localized regions of the northern hemisphere were not unexpected on the basis of earth-based telescopic observations. The constraints on the temporal and spatial coverage by Viking did not lead to sufficiently extensive data on these systems to make a comparison with the "dust storm

years" meaningful. The concentration and seasonal variation of ozone in the dry, cold winter polar regions compare well with Mariner 9 observations; but there are no 1977 data with which to compare the W data.

In addition to what these observations have taught us about Mars, imaging with HST has proved that that instrument, if it were not restricted by the solar elongation constraint, could observe Mars usefully throughout its synodic cycle. When Mars is near opposition the images approach "weather satellite" resolution; for example, the detail in the structure of the north polar hood, despite unfavorable geometry, is comparable to Mariner 9 wide angle observations. Even when Mars' angular size was less than 5 arc sec, the images were comparable to good earth-based photography near oppositions. The ability of WFPC to sample the W part of the spectrum has also proved invaluable; the ability of WFPC2 to monitor planetary ozone can add an extra dimension to photochemical studies during the Mars Observer studies in 1994 and 1995. This particular capability was lost during Cycle 2 due to contamination with W-opaque substances. Visible imaging of Mars and FOS observations have continued during Cycle 2 emphasizing coincident seasonal observations. This will provide detailed comparisons between two different martian years which will be reported in a future publication.

Acknowledgements

We gratefully acknowledge the support of Space Telescope Science Institute through grant number 3107. In addition, we wish to thank Dr. Riccardo Giacconi, Director of STScI, who permitted the execution of our program as the first GO program on HST. Special thanks go to many personnel at STScI who guided us through the difficulties of **deconvolution** and data reduction while the system was still in development. We especially wish to thank John Mackenty, Marc Buie, Dan Golombek, and James Westphal without whose efforts our success would have been limited. *The work of R. Kuhn and R. Zurek was carried out at JPL/Caltech, under contract with NASA.*

References

- Allen, C.W. 1973. *Astrophysical Quantities, 3rd Edition*, Oxford University Press, New York, NY.
- Barth, C.A., C. W. Herd, A. I. Steward, A. L. Lane, M. L. Dick, and G. P. Anderson 1973. Mariner 9 ultraviolet spectrometer experiment: Seasonal variation of ozone on Mars. *Science* 179, 795-796.
- Briggs, G.A., and C.B. Leovy 1974. Mariner 9 observations of the Mars north polar hood. *Bull. Amer. Meteorol. Soc.* 55, 278-296.
- Capen, C.F. and V.W. Capen 1970. Martian north polar cap, 1962-1968. *Icarus* 13, 100-108.
- Christensen, P.R. 1988. Global albedo variations on Mars: Implications for active aeolian transport, deposition, and erosion. *J. Geophys. Res.* 93, 7611-7624.
- Clancy, R. T. and S. W. Lee 1991. A new look at dust and clouds in the Mars atmosphere: Analysis of emission-phase function sequences from global Viking IRTM observations. *Icarus* 93, 135-158.
- Clancy, R.T., D.O. Muhleman, and G.L. Berge 1990. Global changes in the 0-70 km thermal structure of the Mars atmosphere derived from 1975 to 1989 microwave CO spectra. *J. Geophys. Res.* 95, 14543-14554.
- Colburn, D.S. 1988. Data set available through the Planetary Data System. PDS dataset id VL1/VL2-M-LCS-5-ATMOS-OPTICAL-DEPTH-V1.0.
- Colburn, D.S., J.B. Pollack, and R.M. Haberle 1989. Diurnal Variations in Optical Depth at Mars. *Icarus* 79, 159-189.
- DeMore, W.B., M.J. Molina, S.P. Sander, D.M. Golden, R.F. Hampson, M.I. Kurylo, C.J. Howard, and A.R. Ravishankara 1990. Chemical kinetics and photometrical data for use in stratospheric modeling. *JPL Publication 90-20*, Pasadena, CA.
- DeMottoni, G. 1975. The appearance of Mars from 1907 to 1971: Graphic synthesis of photographs from the I.A.U. Center at Meudon. *Icarus* 25, 296-332.
- Hess, S. L., R. M. Henry, C. B. Leovy, J. A. Ryan, and J. E. Tillman 1977. Meteorological results from the surface of Mars: Viking 1 and 2. *J. Geophys. Res.* 82, 4559-4574.
- Herd, C. W., K.E. Simmons, and L. K. McLaughlin 1974. Mariner 9 ultraviolet spectrometer experiment: Pressure-altitude measurements on Mars. *Icarus* 21, 292-302.
- Hunt, G.E., A.O. Pickersgill, P.B. James, and G. Johnson 1980. Some diurnal properties of clouds over the Martian volcanoes. *Nature* 286, 362-364.
- Iwasaki, K., Y. Saito, and T. Akabane 1979. Behavior of martian north polar cap, 1975-1978. *J. Geophys. Res.* 84, 8311-8316.
- Iwasaki, K., Y. Saito, and T. Akabane 1982. Seasonal change of martian north polar cap, 1979-80. *J. Geophys. Res.* 87, 10,265-10,269.
- Jakosky, B.M. 1986. On the thermal properties of martian fines. *Icarus* 66, 117-124.
- Jakosky, B.M. and T.Z. Martin 1987. Mars: North polar atmospheric temperatures

during dust storms. *Icarus* 72, 528-534.

James, P.B. 1979. **Recession** of Martian north polar cap: 1977-1978 **Viking** observation. *J. Geophys. Res.* 84, 8332-8334.

James, P.B. 1982. **Recession** of Martian north polar cap: 1979-1980 **Viking** observations. *Icarus* 52, 565-569.

James, P.B., R.T. Clancy, S.W. Lee, L.J. Martin, R.B. Singer, R. Kahn, and R.W. Zurek 1991. **Observations of Mars using Hubble Space Telescope** observatory. *The first year of HST observations* (A.L. Kinney, and J.C. Blades, Eds.), 161-178. Space Telescope Science Institute, Baltimore, MD.

James, P.B., L.J. Martin, J.B. HenBon, and P.V. Birch 1990. Seasonal recession of **Mars'** south polar cap in 1986. *J. Geophys. Res.* 95, 1337-1341.

Kahn, R. 1983. Some observational constraints on the global **scale** wind **systems of Mars**. *J. Geophys. Res.* 88, 10189-10209.

Kieffer, H.H., T.Z. Martin, A.R. Peterfreund, B.M. Jakosky, E.D. Miner and F.D. Palluconi 1977. Thermal and **albedo** mapping of Mars during the Viking primary mission. *J. Geophys. Res.* 82, 4249-4295.

Kong, T. Y., and M. B. McElroy 1977. Photochemistry **of** the Martian atmosphere. *Icarus* 32, 168-189.

Lauer, T.R. 1989. The reduction of wide field / planetary camera images. *PASP* 101, 445-469.

Lee, S.W., P.C. Thomas, and J. Veverka 1982. Wind streaks in **Tharsis** and **Elysium**: Implications for sediment transport by slope winds. *J. Geophys. Res.* 87, 10025-10042.

Lucy, L.B. 1974. An iterative technique for the rectification of observed distributions. *Astronomical Journal* 79, 745-754.

MacKenty, J. W., R. E. Griffiths, W. B. Sparks, K. Home, R. Gilmozzi, S. P. Ewald, C. E. Ritchie, S. M. Baggett, L. W. Walter, and G. Schneider 1992. **Hubble Space Telescope Wide Field-Planetary Camera Instrument Handbook**, Version 3.0, April 1992, Space Telescope Science Institute, Baltimore, MD.

Martin, L.J. and W.A. Baum 1978. A study of cloud motions on Mars. Final Report B under **JPL Contract 951547**. Lowell Observatory, Flagstaff, AZ.

Martin, L.J. and W.M. McKinney 1974. North polar hood **of Mars** in 1969 (May 18-July 25) I: Blue light. *Icarus* 23, 380-387.

Martin, L.J. and R.W. Zurek 1993. An **analysis** of the **history** of dust activity on Mars. *J. Geophys. Res.* 98, 3221-3246.

Moroz, V.I., E.V. Petrova, L.V. Ksanfomality, O.F. Ganpantzerova, J.P. Bibring, M. Combes, and A. Soufflot 1991. characteristics of aerosol phenomena in the martian atmosphere from **KRFM** experiment data. *Planet. Space Sci.* 39, 199-207.

Pang, K., and J. M. Ajello 1977. Complex refractive **index of Martian dust**: wavelength dependence and composition. *Icarus* 30, 63-74.

Pleskot, L.K., and E.D. Miner 1981. Time variability of martian **bolometric albedo**. *Icarus* 45, 179-201.

Sagan, C., J. Veverka, P. Fox, R. Dubisch, R. French, P. Gierasch, L. Quaint J. Lederberg, E. Levinthal, R. Tucker, B. Eross and J.B. Pollack 1973. Variable features on **Mars**, 2, Mariner 9 global results. *J.*

Geophys. Res. 78, 4163-4196.

Schaber, G.G. 1982. **Syrtis Major: A Low-Relief Volcanic Shield.** *J. Geophys. Res.* 87, 9852-9866.

Simpson, R.A., G.L. Tyler, and D.B. Campbell 1978. **Arecibo radar observation of martian surface characteristics** near the equator. *Icarus* 33, 102-115.

Slipher, E.C. 1962. *The Photographic Story of Mars.* 168 pp., Northland Press, Flagstaff, AZ.

Smith, S.A., and Smith, B.A. 1972. Diurnal and **seasonal** behavior of discrete white clouds on Mars. *Icarus* 16, 509-521.

Stamnes, K., S.C. Tsay, W. Wiscombe, and K. Jayaweera 1988. Numerically stable algorithm for discrete ordinate method radiative transfer in multiple scattering and emitting layered media. *Appl. Optics* 27, 2502-2509.

Thomas, P., and J. Veverka 1979. Seasonal and secular variation of wind streaks on Mars: An **analysis** of Mariner 9 and Viking data. *J. Geophys. Res.* 84, 8131-8146.

Thomas, P., J. Veverka, S. Lee, and A. Bloom 1981. Classification of wind **streaks** on Mars. *Icarus* 45, 124-153.

Wide Field / Planetary Camera Investigation Definition Team 1991. *Wide Field / Planetary Camera final orbital / science verification report.* Space Telescope Science Institute, Baltimore, MD.

Table I

Filter Properties

Filter	$\langle\lambda\rangle$ (rim)	$\Delta\lambda$ (rim)	Exposure	Comment
F230W	231.3	36.6	2.0m	Hartley O ₃
F336W	336.0	41.1	3.0s*	
F439W	435.2	46.5	0.26s	Only used 12-90
F413M	412.5	24.8	1.4s	Standard Violet
F502N	501.8	2.9	2.0s	
F588N	588.0	4*3	0.7s	Only used 12-90
F673N	672.3	5.0	0635s	Standard Red
F889N	888.8	5.1	0.6s	Only used 12-90

*adjusted after **initial** exposures

Table II
Observations

Date	L _r	LCM Diameter	e_{SE}	Filters
12-13.78-90	348.7	302 16.31	-11.9	A
12-14.11-90	348.9	61 16.28	-12.0	A
01-02.23-91	358.7	290 13.55	-13.2	C, UV
02-07.20-91	16.2	305 9.31	-10.1	S, UV
03-20.28-91	35.2	302 6.60	- 1.8	s
05-14.71-91	59.9	283 4.84	+11.8	C, UV
05-15.05-91	60.0	43 4.83	+11.9	s
05-15.39-91	60.2	161 4.82	+11.9	s

S=F413M and F673N;C=S plus F502N;W=F230W and F336W;A=complete set

Table III

Cloud	θ_{inc}	em	ϕ	I_{MAX}	LCM
Alba PM	25.8	54.6	33.3	2050	161
Elysium PM	28.6	61.6	33.1	2600	283
Tithonius PM	43.4	73.9	33.3	2400	161
Arabia PM	29.6	62.6	33.2	1700	43
Alba AM	81.4	63.6	33.2	1400	43
Elysium AM	81.5	55.6	33.3	1050	161
Tithonius AM	75.4	43.1	33.2	1350	43
Arabia AM	81.8	54.2	33.1		283

Table IV		
Observational Parameters	December 13, 1990	May 14, 1991
Solar Longitude	348° (late northern winter)	59° (northern spring)
Angular Diameter	16.5"	4.9"
Spatial Resolution	'80 km	'270 km
Sub Earth Lat	12° s	11.5° N
Sub Solar Lat	5° s	22° N
Central Meridian	303° w	285°
Sub Earth Local Time	11:15 PM	9:45 AM

TABLE Va December 13, 1990 (L, = 348°)		
Latitude	Cloud Opacity	Ozone Column (mm-atm)
62°N	(polar hood) .14	18
55° N	.22	12
50° N	.24	9
47° N	.22	≤6
45° N	.04 (morning)	
40-60° S	.05	
60° S		≤6
65° S		9
70° S		12

Table Vb May 14, 1992 (L, = 59°)		
Latitude	Cloud Opacity	Ozone Column (mm-atm)
75° N		18
70° N	seasonal ice cap	13
65° N	(table VI)	12
60° N		9
30°S-500 N	(Arabia & Elysium Planitia) 0.1-0.2	not constrained
20°-300 N	(Elysium Mons) 0.2-0.4	
30° S		≤ 6
35° S	02	9
40° S	:08	12

TABLE VI		
Mars Ultraviolet Albedoes		
	230 nm	330 nm
surface (no distinction between bright and dark regions)	.01	.02
north seasonal ice cap (function of latitude)		
75° N	.13	.15
70° N	.13	.15
65° N	13 *	15
60° N	:08	:09
55° N	.04	045
≤50° N	.01	:02

Figure Captions

Figure 1. HST Cycle 0 images of Mars. The images have been rotated so that geographic North is to the top, and are shown at the correct relative size (Calendar date, L_s , and apparent diameter of Mars are annotated). The images on the left were obtained through WF/PC's F439W (Dec90) or F413M (all other times) filter; the images on the right were obtained through the F673N filter.

Figure 2. Images of Mars acquired in December of 1990, a few days after opposition, are shown in for F439W (left) and for F673N (right) for the Syrtis Major region (top) and for the Valles Marineris face (bottom). Because the latter two images were acquired on consecutive orbits of HST, there is a difference in the central meridians of the two images; the longitude of central meridian for the 673N image of Valles Marineris is 84.3 degrees west. Great detail is seen of the region to the north of the Valles Marineris canyon system
...

Figure 3. Flat fielded and deblurred version of the 673N image of the Solis Lacus region of Mars acquired in December, 1990, near opposition is compared to a version upon which eighty iterations of the Lucy-Richardson have been performed. Forty to eighty iterations generally optimized resolution without greatly increasing the background noise.

Figure 4. The effects of the Richardson Lucy deconvolution algorithm on an artificially generated planetary image with a sharply defined albedo feature (a polar cap) are illustrated in this set of three figures. A meridional scan through the "bare" image is shown in a); some darkening was included at the limbs of the planet and noise was added using the IRAF routine MKNOISE. The image in b) is the two dimensional convolution of this image with the 673N point spread function; this represents the "raw" image of a) which would be recorded by the Planetary Camera. The scan shown in c) is the image in b) deconvolved with the same PSF using forty iterations of the Richardson Lucy. The actual limbs of the planet occur at roughly 15% of the maximum intensity; photometric accuracy is preserved; and the correct location of the true edge of the "polar cap" is halfway between maximum and minimum intensities.
procedure.

Figure 5. An enlargement of the portion of the north polar hood seen in the 413M image of the Valles Marineris region acquired in December, 1990, is shown in this figure. As described in the text, the extension of the hood into the Tempe region and the relatively unclouded appearance of the cap core are features which make this image of particular interest.

Figure 6. From top to bottom this figure displays the 413M (left) and 673N (right) images acquired in May, 1991, with central meridians of 283, 43, and 161 degrees longitude.

Figure 7. This contour plot of the afternoon limb of the 413M image centered at 161 degree longitude clearly shows three primary clouds located near Alba Patera, Tithonus, and Ascraeus Mons.

Figure 8. Filter transmission profiles for the HST 230W and 336W filters versus the ozone absorption cross section in the Hartley band. When both the filter and ozone cross section are convolved with the solar flux and Rayleigh cross section, the effective ozone absorption becomes 10-100 times less in 336W versus 230W images of Mars.

Figure 9. Processed 230W and 336W images of Mars obtained with HST on December 13, 1990 and May 14, 1991. The apparent size of Mars

decreased from 16.5 to 4.9 **arcseconds** over **this** period. The third **set** of images present the image ratio of the 230W and 336W images. Dark **regions** near the poles in these ratio images indicates ozone absorption in the 230W images.

Figure 10. Polar (north-south) cross sections of the December 13, 1990 230W and 336W **images** of **Mars**. Both cross **sections** are presented in reflectance, normalized to the standard model (heavy solid line) at the disk center. Both of the 230W and 336W model profiles include a north polar hood of opacity 0.2 (see text). The 230W **dashed** line model indicates the effect of ozone absorption for a latitude dependent ozone column peaking at 18 urn atm in the north. No dust **is** incorporated in either of the models.

Figure 11a. Equatorial (east-west) cross section of the December 13, 1990 230w image of **Mars**. The **brightness** units are presented **as** reflectance, in which the disk center **pixels** have been normalized to a model reflectance (see text). The heavy solid line represents a clear, Rayleigh scattering atmosphere over a moderately limb darkened constant **albedo** surface, which **best fits** the observed limb brightening. Two additional models include ozone absorption (dotted) and dust scattering/absorption (dashed), which **underpredict** the observed limb darkening. **All** of the models have been normalized to agree with the standard model (heavy solid line) near the disk center.

Figure 11b. Same **as** for Figure 11a, except for the 336w image of **Mars** in December 13 of 1990. The ozone absorption **case is** not shown **since** ozone **absorbs** negligibly **in this** filter.

Figure 12. Polar (north-south) **cross** sections of the May 14, 1991 230W and 336w images of **Mars**. These **observations** have been normalized to the model at northern and southern **mid-latitudes**, **as** significant cloud opacities are present over the **centers** of the images. These Arabia clouds are roughly **modelled** by opacities near 0.2, **as** indicated by the light dotted **lines**. South polar **clouds** of opacity 0.1 and a north polar surface ice of **albedo** 0.1-0.15 are incorporated in the heavy solid line model. Ozone absorption in the 230w **cross section is** fit by ozone columns of 9-18 urn atm (see table V) , **as** indicated by the heavy **dashed** line profiles near the poles.

Figure 13a. Equatorial (east-west) **cross** sections of the May 14, 1991 230W image of **Mars**. Normalization of the image reflectance to the **model** reflectance is the same as for **Figure** 12. The significant cloud opacities over Arabia and **Elysium** are **distinguished** by the **Rayleigh** scattering (dotted) versus the Rayleigh **plus** cloud scattering (solid) models.

Figure 13b. Same **as** for figure 13a, for **the** 336w image.

Figure 14. Optical depth of the martian atmosphere **as** a function of time for the **first** two **Mars** years of the **Viking** mission. optical depth measurements were derived from Viking Lander **observations** [Colburn et al, 1989]. The plots were **made from** data contained in the data **set** Colburn (1988).

Figure 15. Viking Orbiter **images** of the **Syrtis** major region. (a) Image 486A50, **Ls=350**, red filter; (b) Image 675A09, **Ls=77**, red filter.

Figure 16. Location map of observations in **single** IRTM mapping sequence covering **Syrtis** Major. **Crosses** indicate the center location of each individual observation's surface footprint.

Figure 17. Maps of Viking **IRTM-derived** Lambert **albedo** of **Syrtis Major** obtained at a variety of times. Maps are in simple cylindrical projection and are displayed with eight **grey-levels** to facilitate tracking **albedo** variations. Observations were binned to a spatial resolution of 2.5 x 2.5 degrees **latitude/longitude**; missing data are **shown as** black.

Figure 18. Maps derived from the HST Cycle 0 F673N **images** of **Syrtis Major**. The maps are displayed with eight grey-levels to facilitate comparison to the Viking **IRTM albedo maps**, Figure 17. The calendar date and **Ls** are annotated.

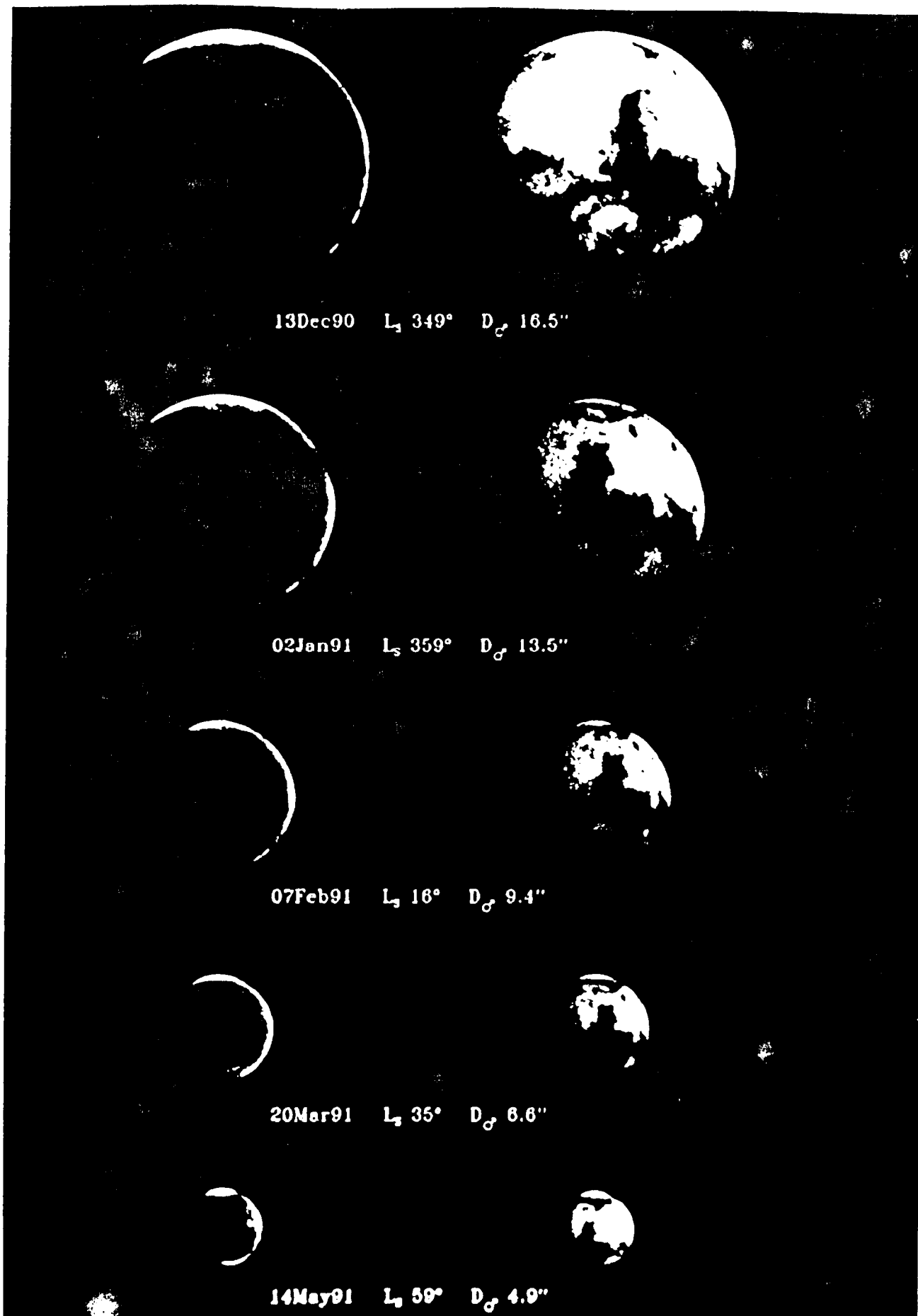


Figure 1



Figure 2

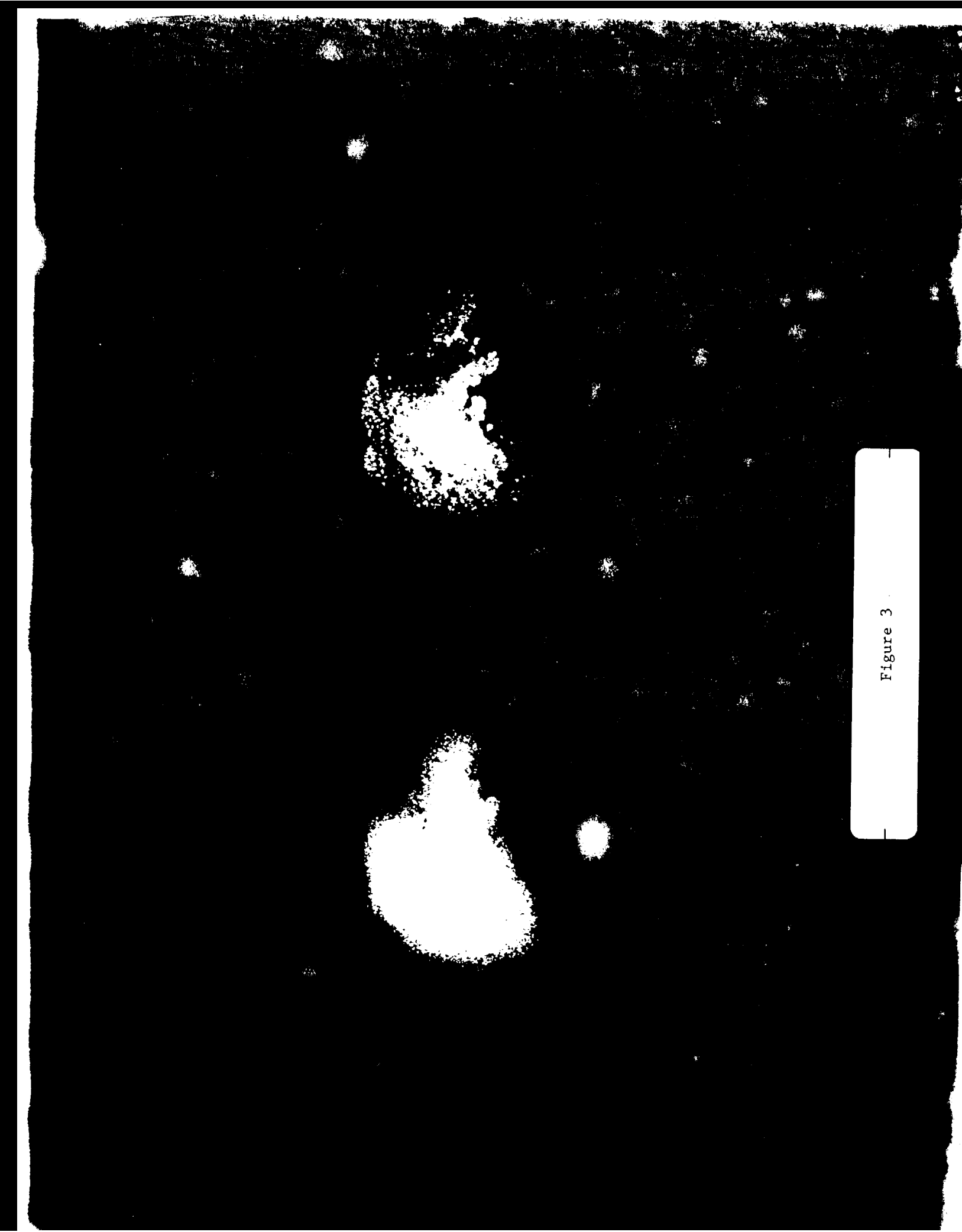


Figure 3

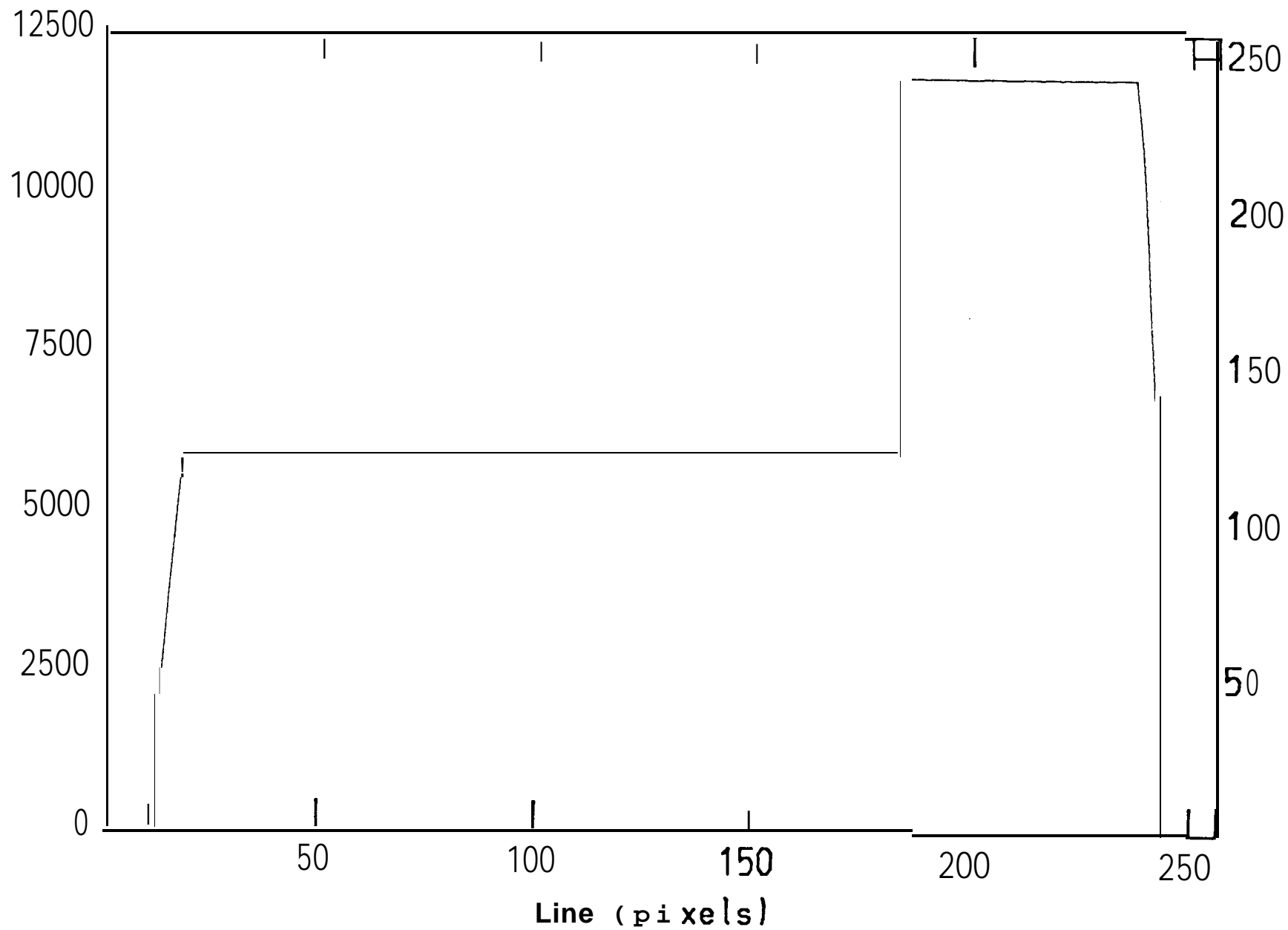


Figure 4 (a)

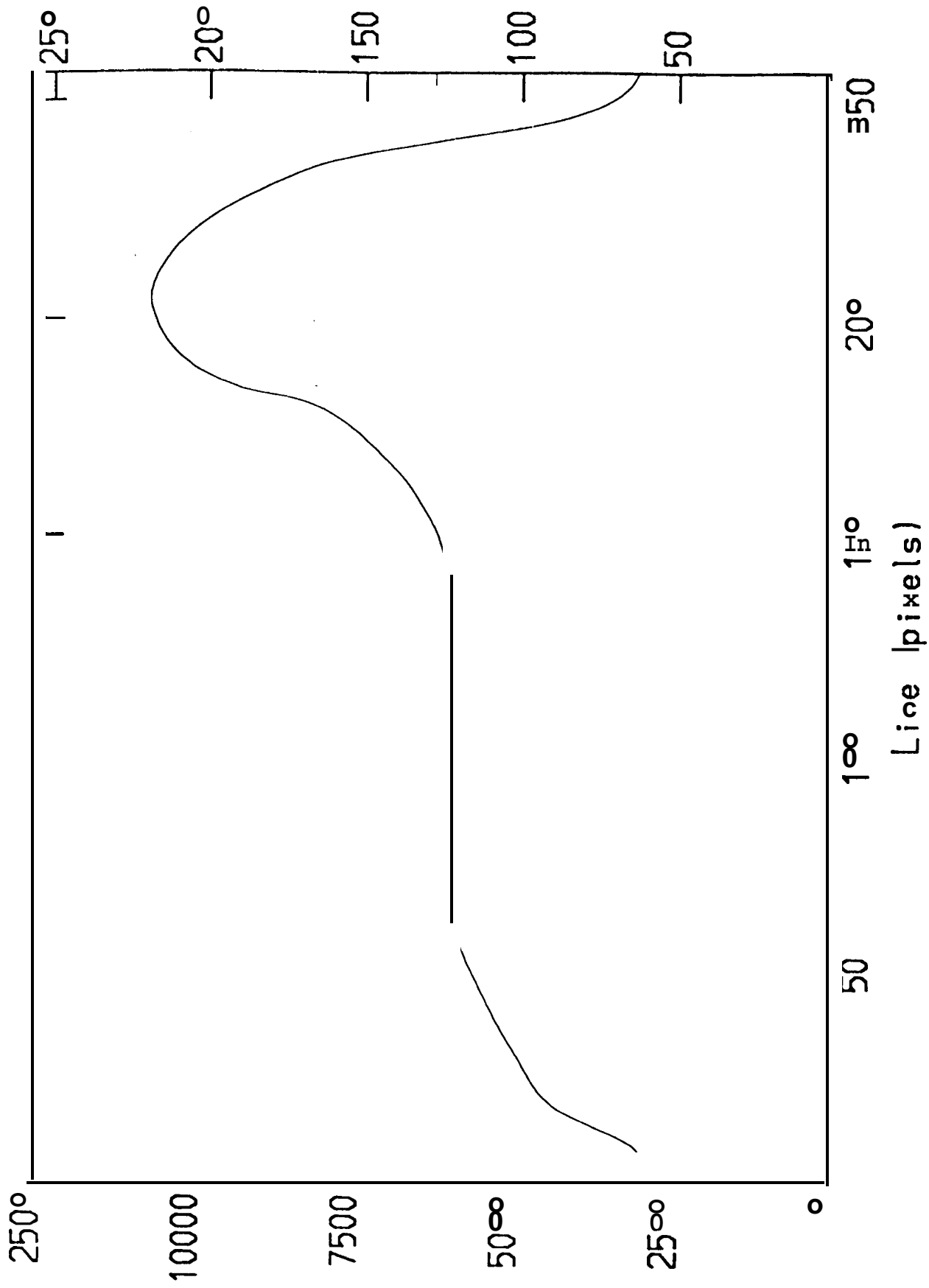


Figure 4 (b)

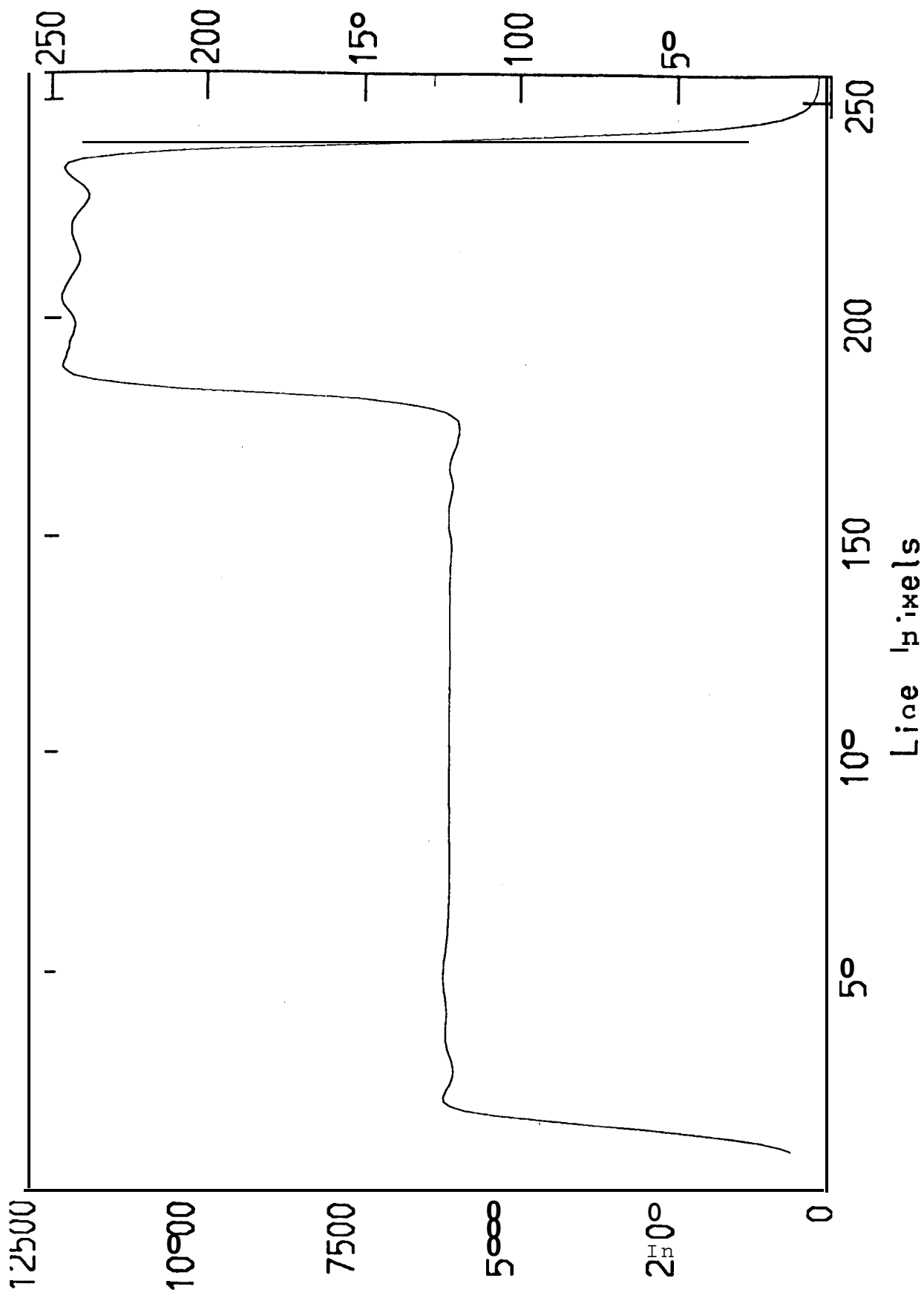


Figure 4 (c)

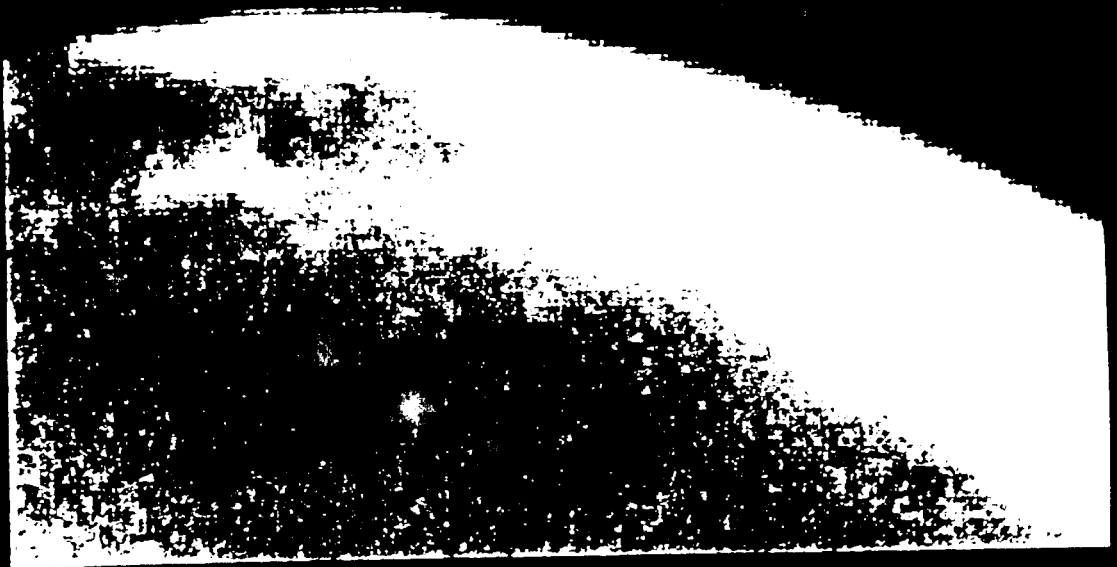


Figure 5

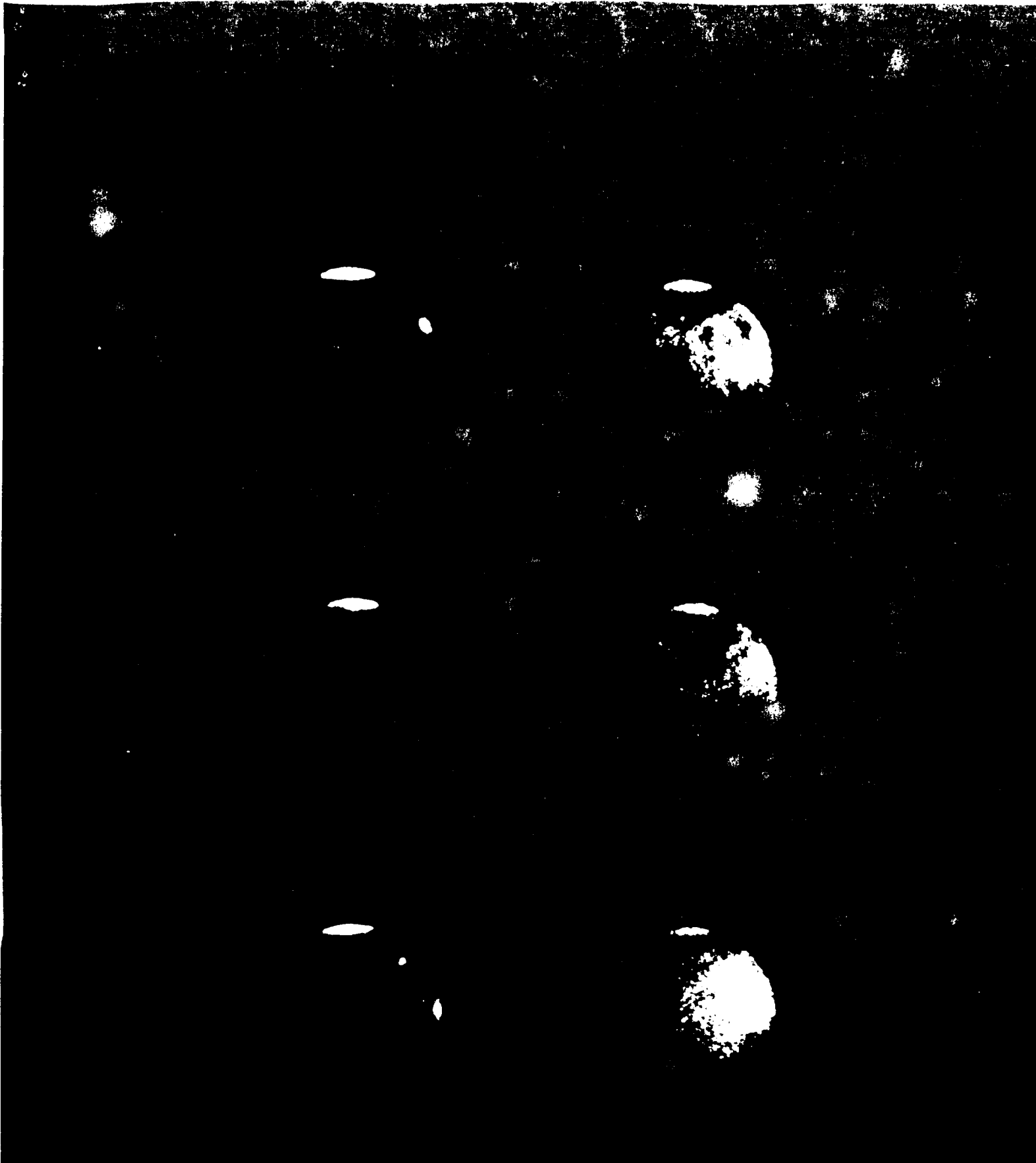


Figure 6

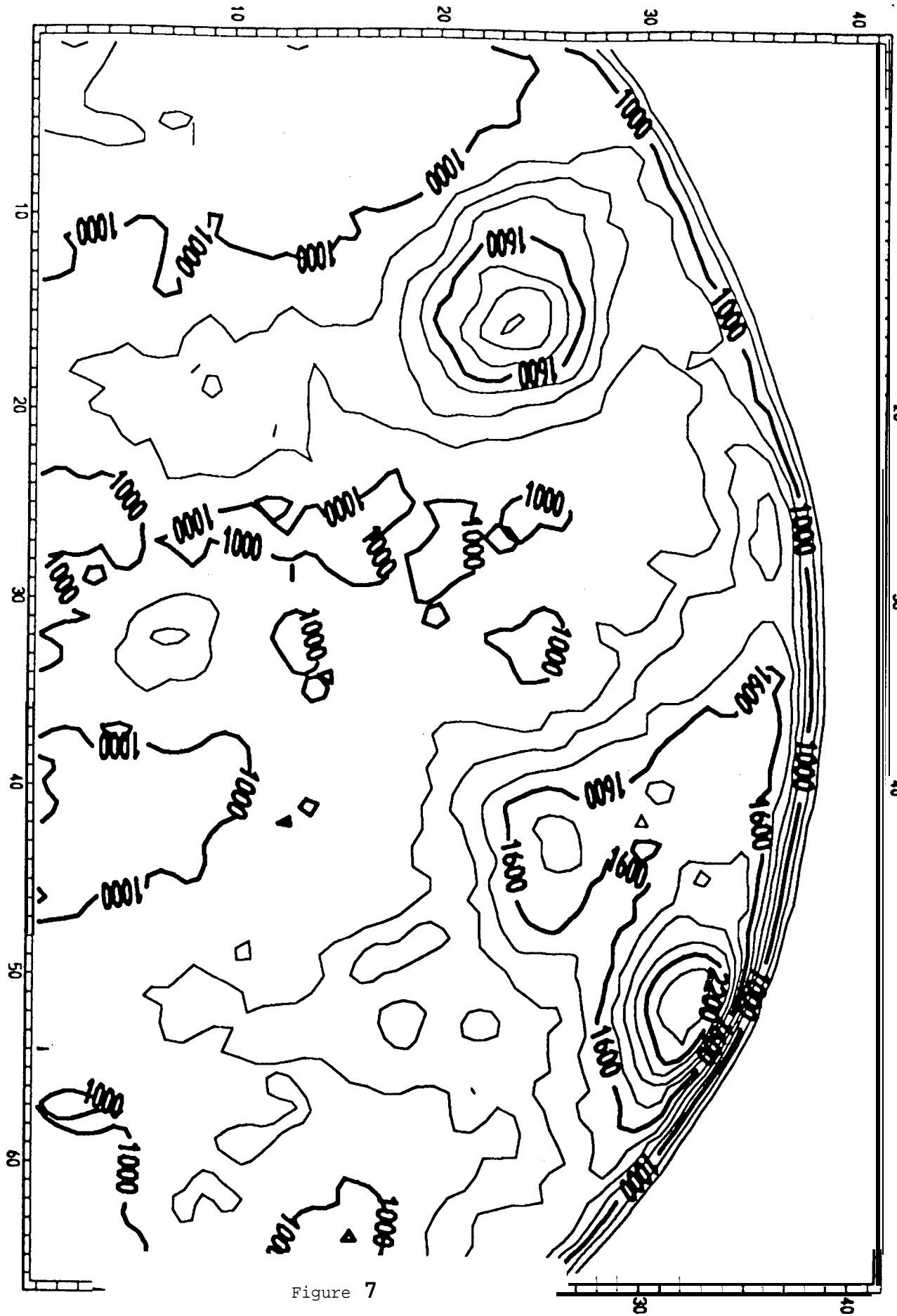


Figure 7

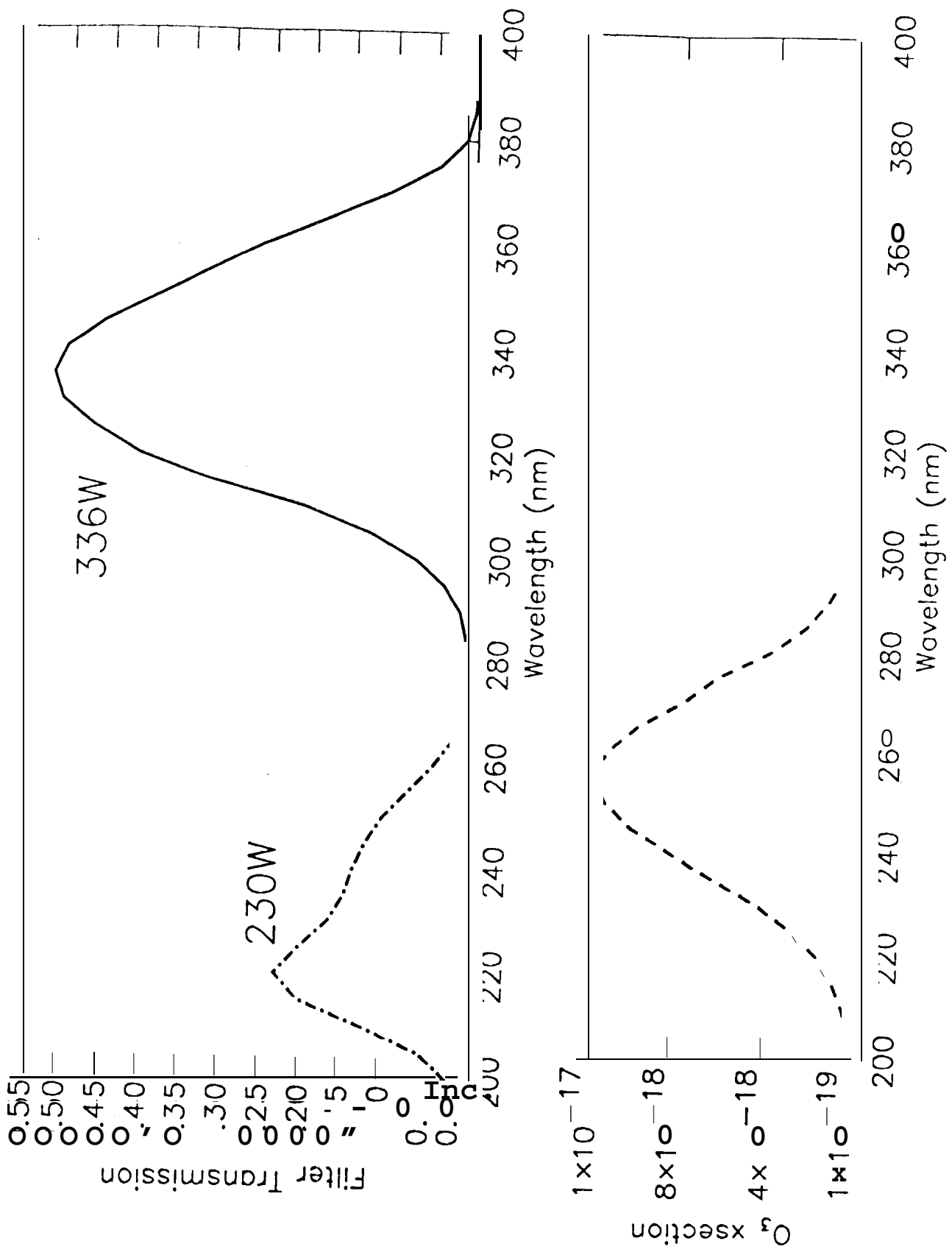


Figure 8

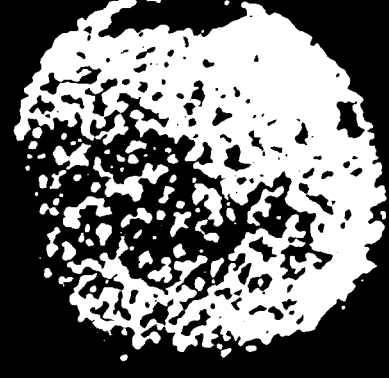
230W



336W



230/336



13Dec90 L_1 349° D_{σ} 16.5"

14May91 L_1 59° D_{σ} 4.9"

Figure 9

December 13, 1990 $L_e = 348^\circ$ $D_s = 6.5''$

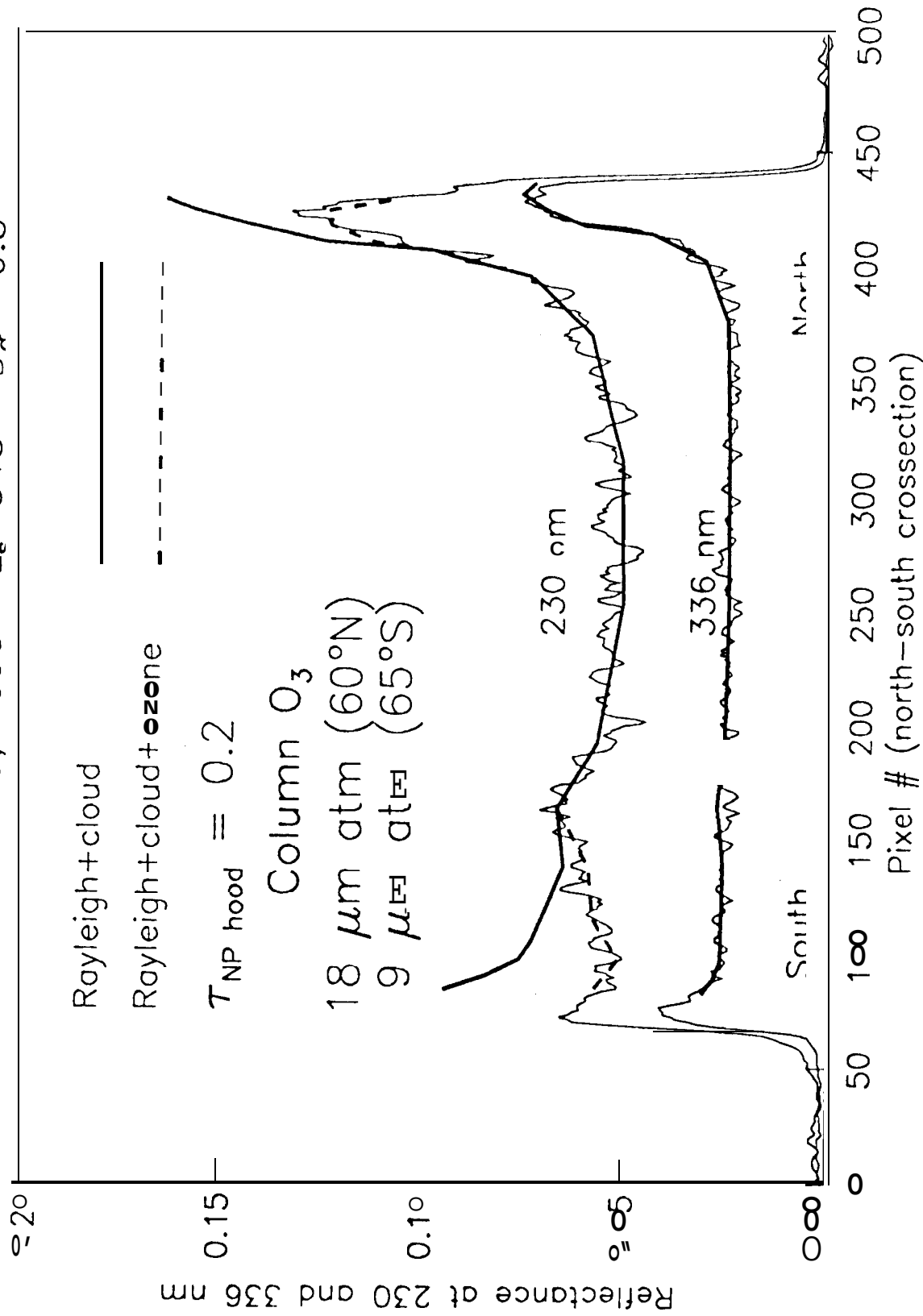


Figure 10

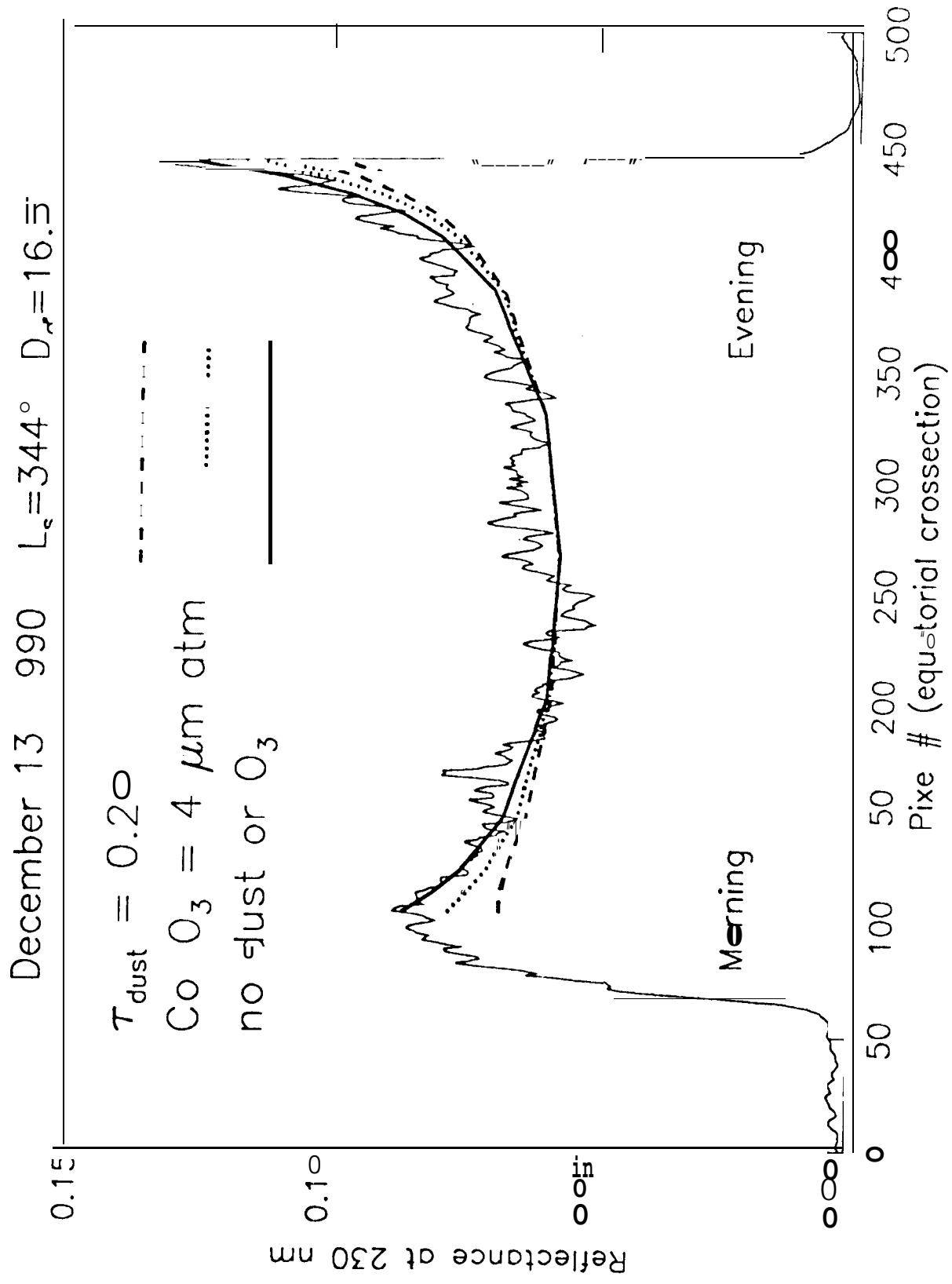


Figure 11 a)

December 13, 1990 L = 344° D. = 16.5"

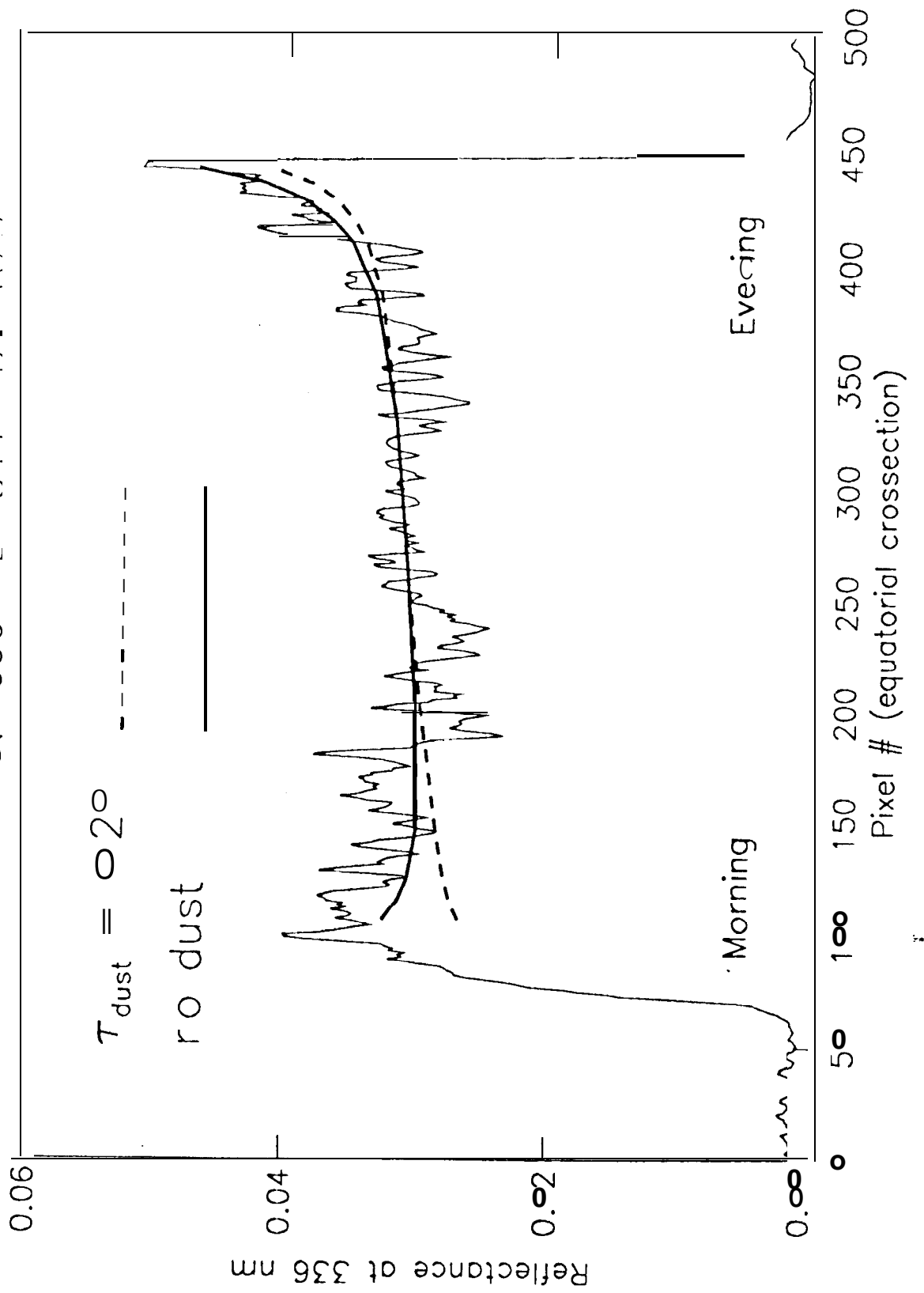


Figure 11 (b)

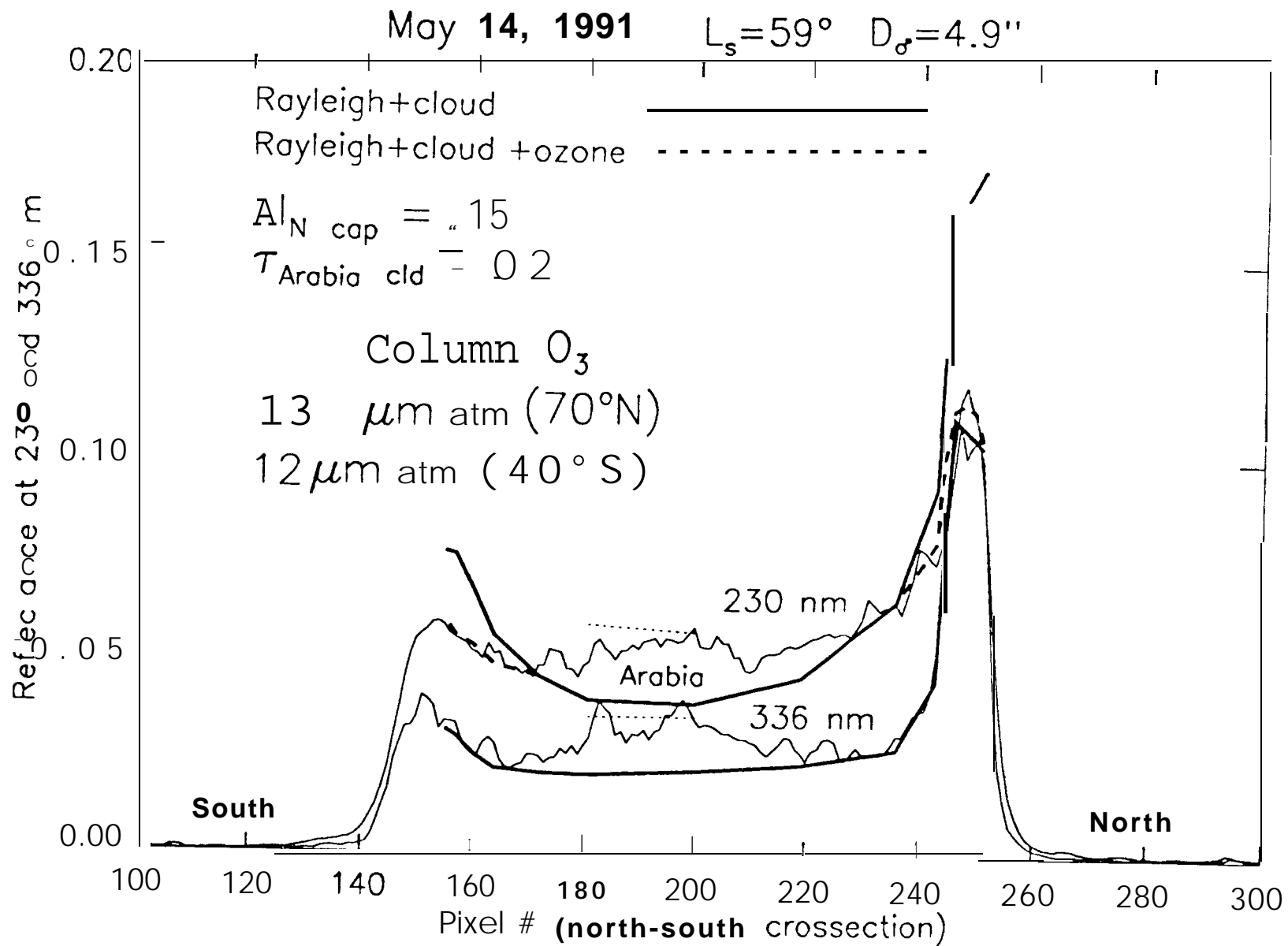


Figure 12

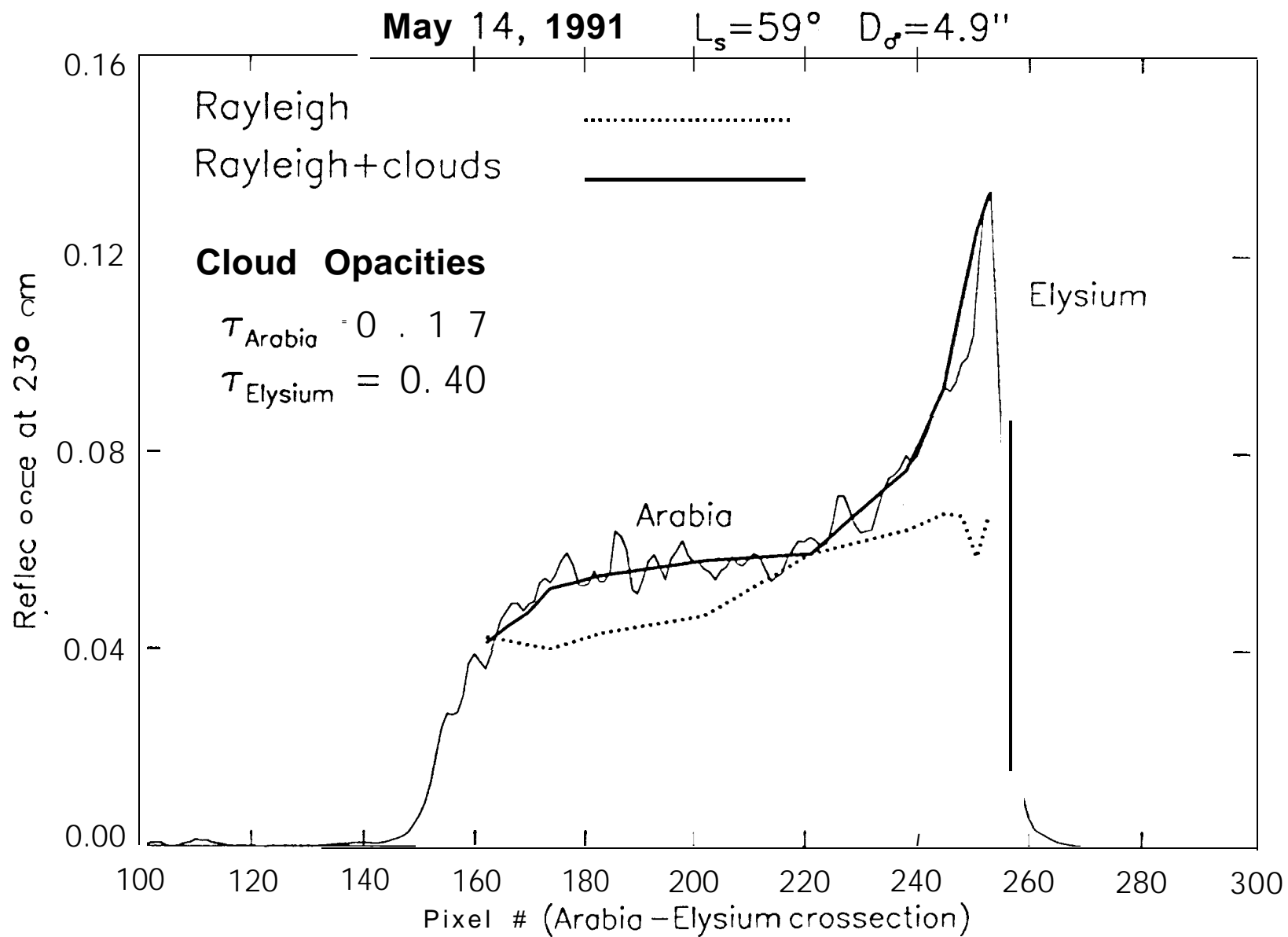


Figure 13 (a)

May 14, 1991 $L_s = 59^\circ$ $D_s = 4.9''$

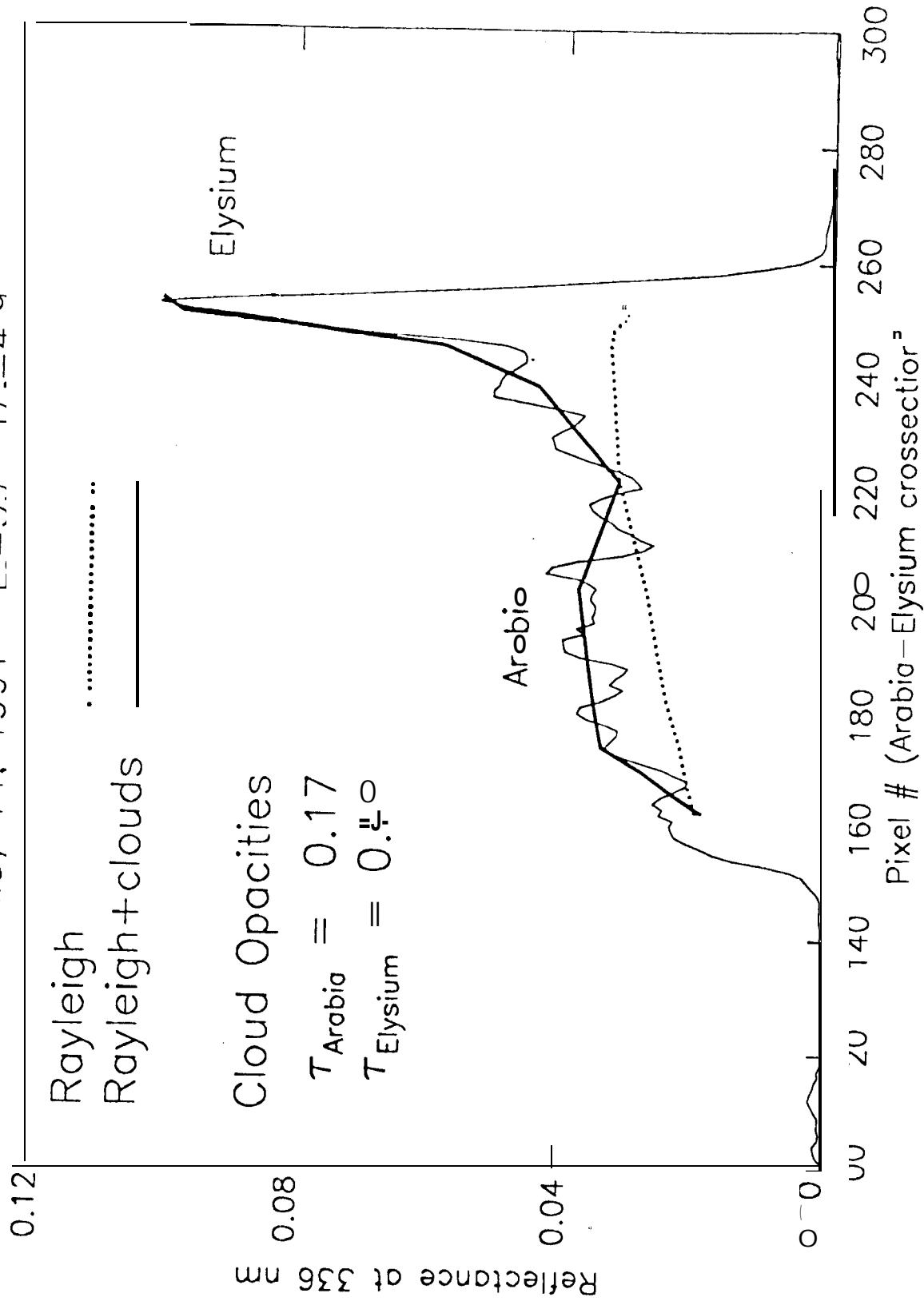


Figure 13 b)

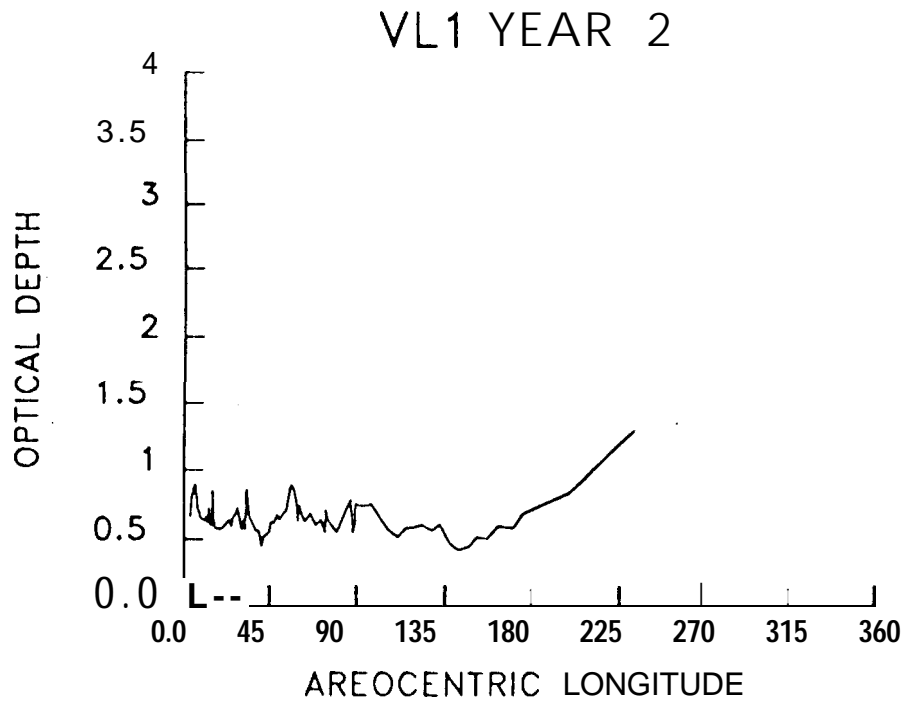
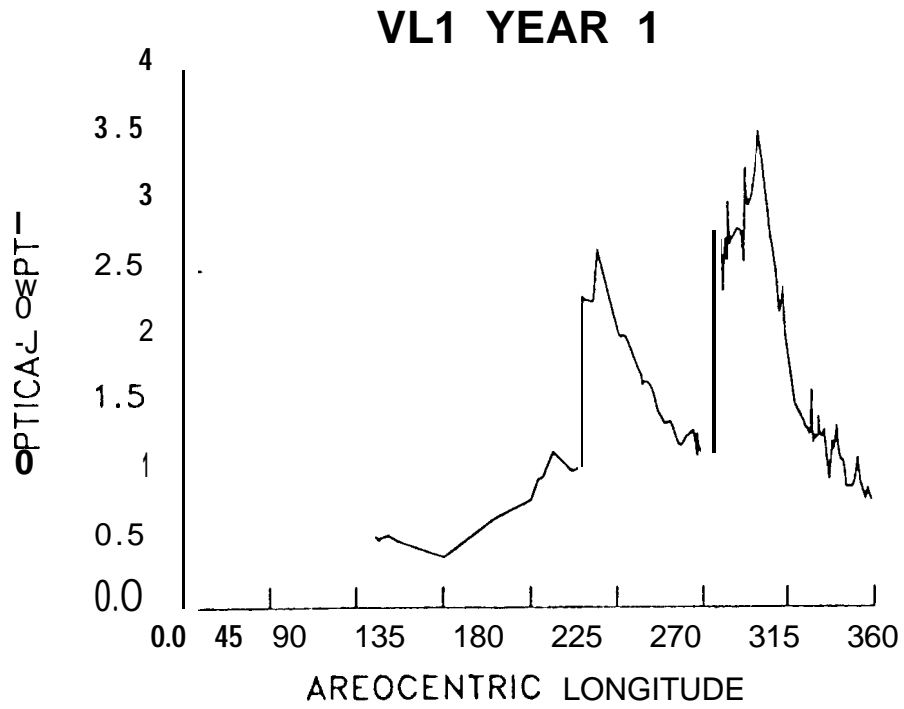


Figure 14



Figure 15 2

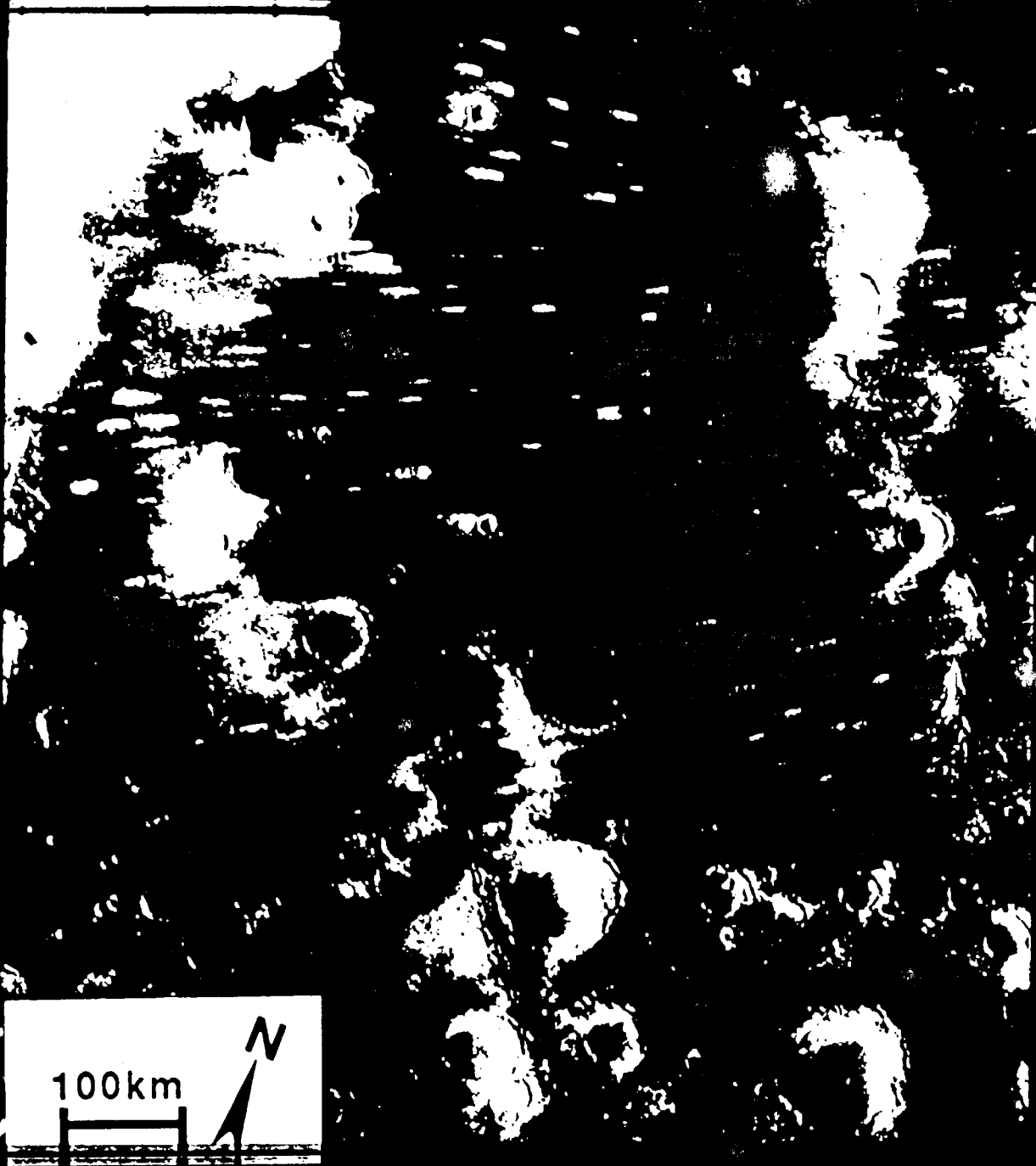


Figure 15 b

LS = 3360.00ORBIT/SEQUENCE: 0498A02
DATA LOCATION MAP
4910 POINTS INCLUDED

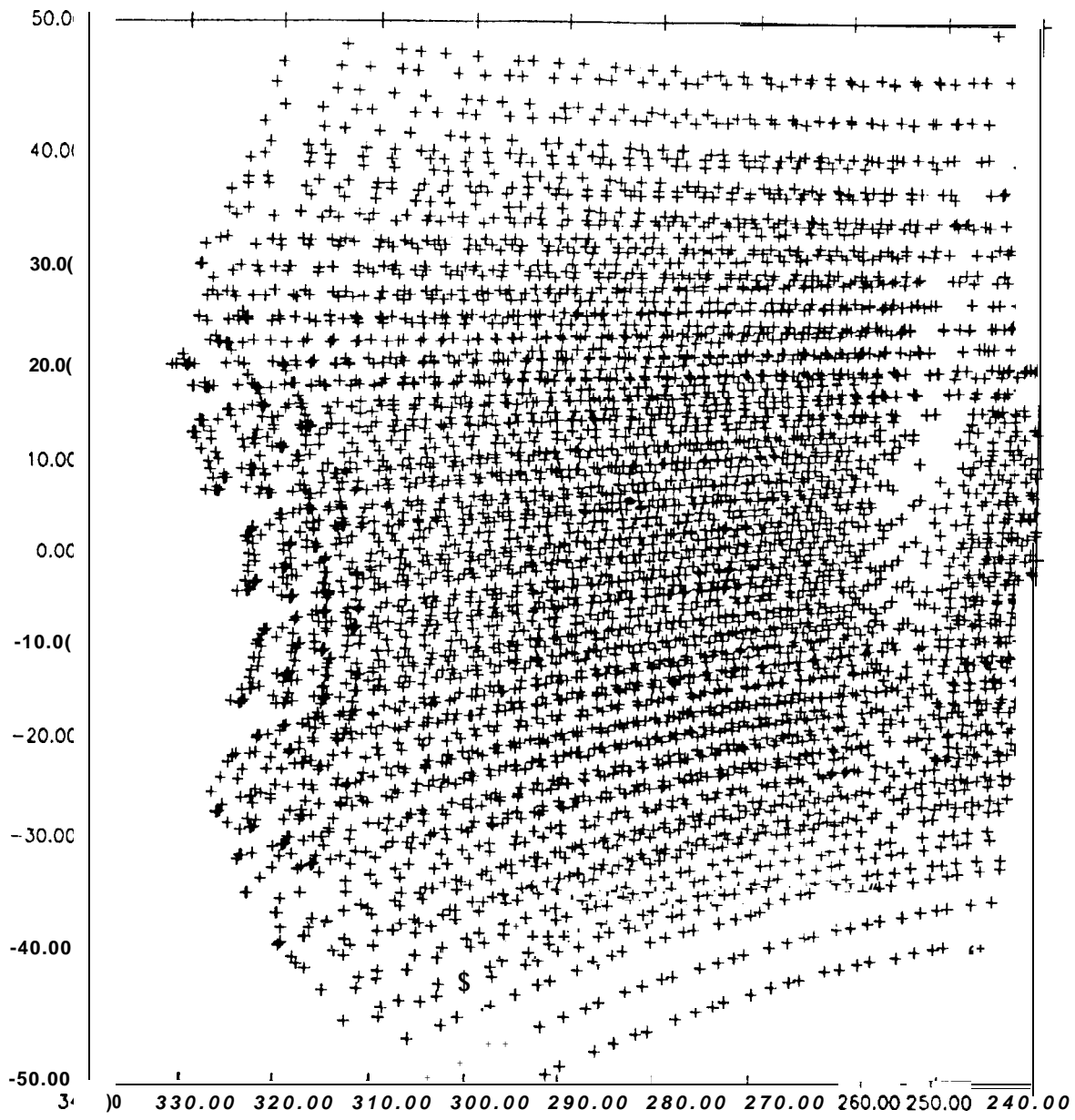


Figure 16

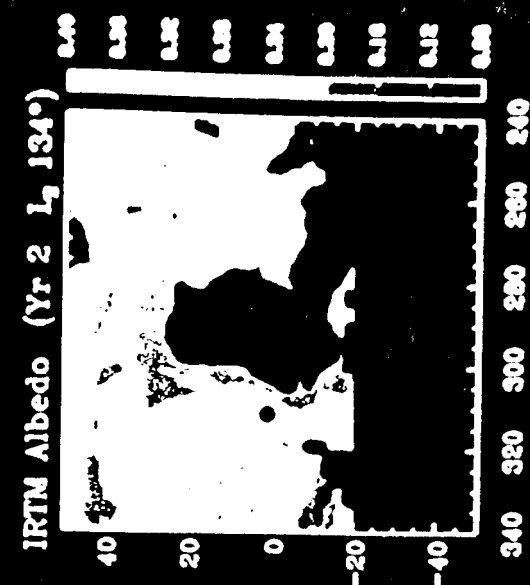
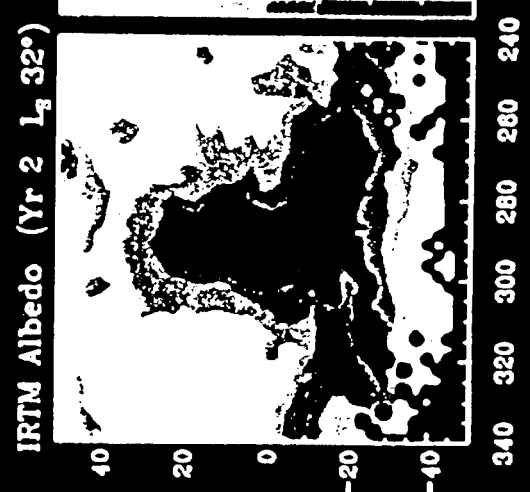
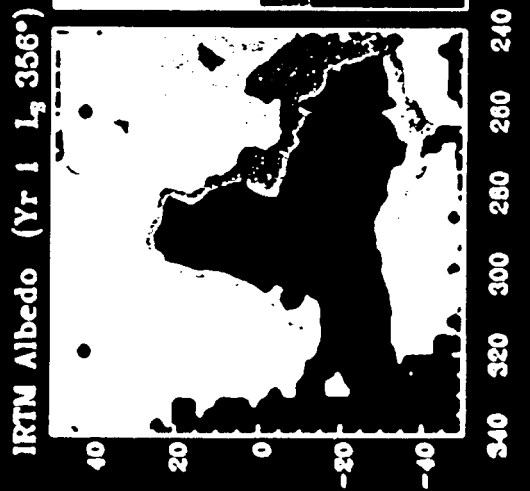
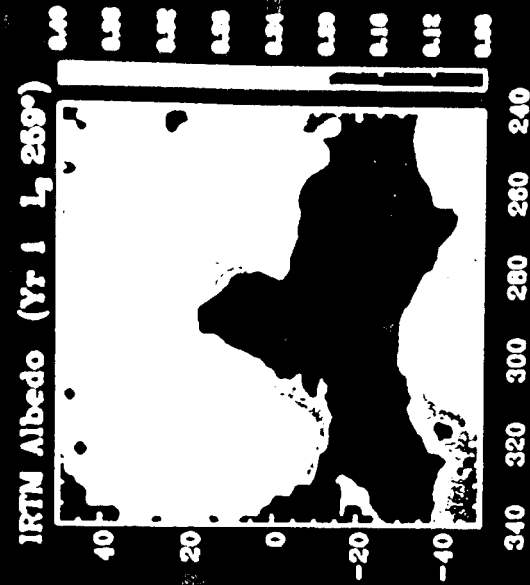
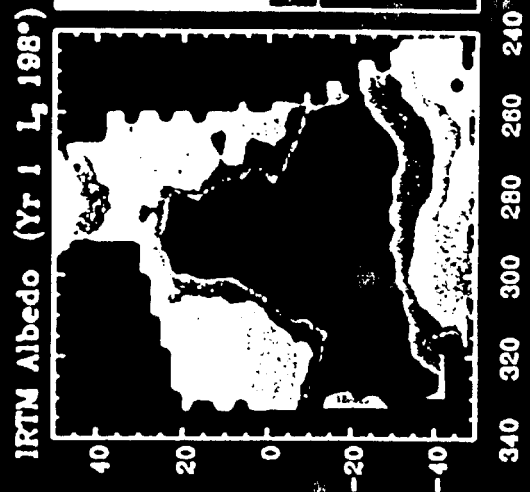
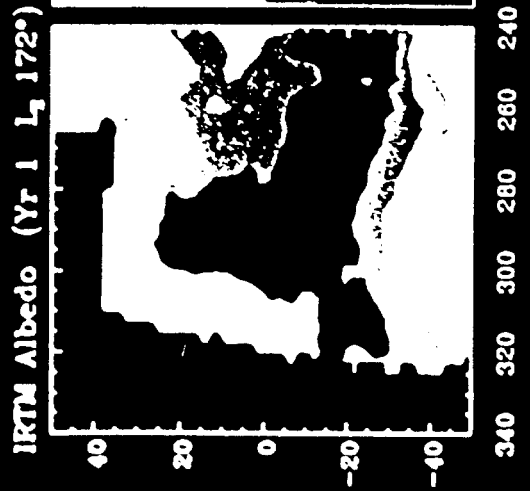


Figure 17

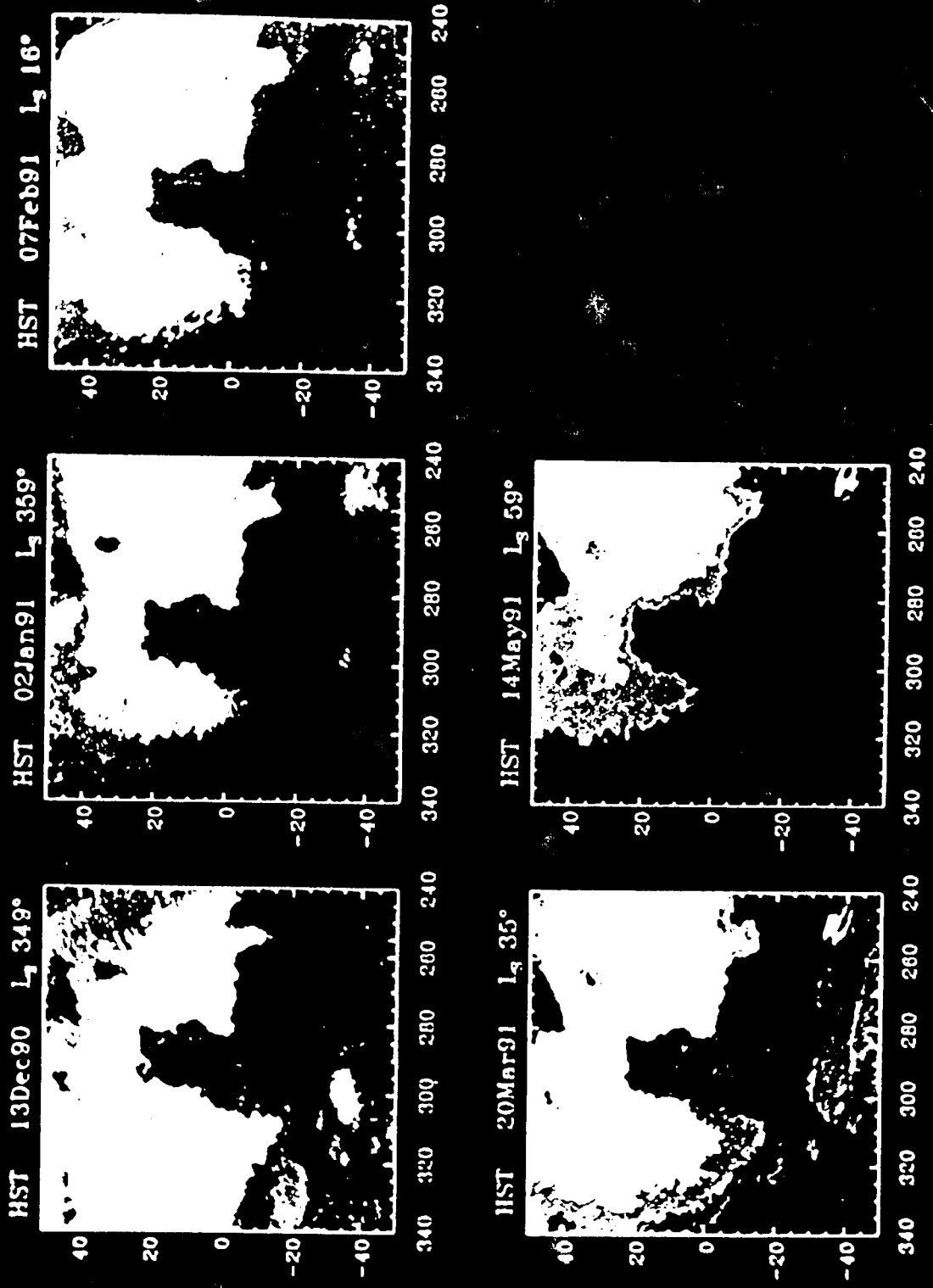


Figure 18